

# Seismic characterization of a fluid escape structure in the North Sea: the Scanner Pockmark complex area

Farid Jedari-Eyvazi<sup>1,2</sup>, Gaye Bayrakci,<sup>2</sup> Timothy A. Minshull,<sup>1</sup> Jonathan M. Bull<sup>1</sup>,  
 Timothy J. Henstock,<sup>1</sup> Calum Macdonald<sup>3</sup> and Adam H. Robinson<sup>1</sup>

<sup>1</sup>*School of Ocean and Earth Science, University of Southampton, Southampton, SO14 3ZH, UK. E-mail: [f.jedari-eyvazi@soton.ac.uk](mailto:f.jedari-eyvazi@soton.ac.uk)*

<sup>2</sup>*National Oceanography Centre, Waterfront Campus, Southampton, SO14 3ZH, UK*

<sup>3</sup>*University of Edinburgh School of Geosciences, Grant Institute, Edinburgh EH93JW, UK*

Accepted 2023 February 13. Received 2023 January 31; in original form 2022 August 16

## SUMMARY

Subsurface fluid escape structures are geological features which are commonly observed in sedimentary basins worldwide. Their identification and description have implications for various subsurface fluid flow applications, such as assuring integrity of overburden rocks to geological CO<sub>2</sub> storage sites. In this study, we applied 3-D first-arrival traveltimes tomography to a densely sampled wide-azimuth and wide-angle ocean bottom seismometer (OBS) data set collected over the Scanner Pockmark complex, a site of active gas venting in the North Sea. Seismic reflection data show a chimney structure underlying the Scanner Pockmark. The objective of this study was to characterize this chimney as a representative fluid escape structure in the North Sea. An area of 6 × 6 km<sup>2</sup> down to a depth of 2 km below sea level was investigated using a regularized tomography algorithm. In total, 182 069 manually picked traveltimes from 24 OBS were used. Our final velocity model contains compressional wave velocity perturbations ranging from −125 to +110 ms<sup>−1</sup> relative to its average 1-D model and compares favourably with a coincident seismic reflection data set. The tomographic velocity model reveals that the chimney as observed in seismic reflection data is part of a larger complex fluid escape structure, and discriminates the genuine chimney from seismic artefacts. We find that part of the seeping gas migrates from a deep source, accumulates beneath the Crenulate Reflector unconformity at ~250 m below seafloor (mbsf) before reaching the porous sediments of the Ling Bank and Coal Pit formation at <100 mbsf. In addition, the model shows that the venting gas at Scanner Pockmark is also being fed laterally through a narrow NW–SE shallow channel. Quantitative velocity analysis suggests a patchy gas saturation within the gas-charged sediments of the Ling Bank and the Coal Pit formations. Confined to the well-resolved regions, we estimate a base case average gas saturation of ~9 per cent and *in-situ* gas volume of ~1.64 × 10<sup>6</sup> m<sup>3</sup> across the Ling Bank and Coal Pit Fm. that can sustain the observed methane flux rate at the Scanner Pockmark for about 10 to 17 yr.

**Key words:** Inverse theory; Controlled source seismology; Seismic tomography; Wide-angle seismic data; Fluid escape structure.

## 1 INTRODUCTION

Characterization of fluid escape structures is of a great importance for de-risking hydrocarbon exploration projects (Berndt 2005; Cartwright *et al.* 2007; Huuse *et al.* 2010), geohazard assessment (Davies 2003), benthic ecosystem studies (Dando *et al.* 1991; Hovland *et al.* 2002; MacDonald *et al.* 2002), estimating geological greenhouse gas emissions (Böttner *et al.* 2019) and the development of geological CO<sub>2</sub> storage projects (Robinson *et al.* 2021), amongst others. More recently, the latter application has received a

great deal of attention as one of the major industrial-scale climate change mitigation options available to meet the 2 °C temperature above pre-industrial levels increase limit of the Paris Agreement. The technical success of geological CO<sub>2</sub> storage depends on several factors including the integrity of overburden rocks, that assures permanent containment of injected CO<sub>2</sub> within geological reservoirs.

Fluid escape structures, such as fractures and remobilized sediments, are highly permeable geological features that breach impermeable sedimentary sequences, creating conduits for focused fluid flow. Seismic observations have exposed many such

structures in sedimentary basins worldwide including those in the North Sea (Karstens & Berndt 2015; Ruge *et al.* 2020). Nevertheless, their internal structures, hydraulic properties, generation mechanisms and timing are poorly understood. They are often found in rapidly deposited, poorly sorted, fine to medium grained clastic deposits (Cartwright & Santamarina 2015), wherein accumulation of impermeable sequences prevents fluid dissipation at the same rate as sediment compaction. As a result, pore pressure increases and when it exceeds the sum of minimum horizontal stress and the tensile strength of the rocks, hydraulic fracturing occurs (Hubbert & Willis 1957). Mandl & Harkness (1987) showed that maximum hydrofracture length for a hard rock is on the order of several tens of metres, while for very soft rocks they reach only to a few metres. Hence, a set of interconnected fractures is required to generate a fractured focused flow system. Leakage through hydrofractures is episodic as fractures open and close with pore pressure fluctuations (Løseth *et al.* 2009). Various generation mechanisms are proposed for fluid escape structures (Cartwright & Santamarina 2015; Yarushina *et al.* 2021), but hydraulic fracturing is the most widely accepted mechanism, at least as an initiator process (Graue 2000; Arntsen *et al.* 2007; Cartwright *et al.* 2007; Løseth *et al.* 2009; Cartwright & Santamarina 2015). Depending on the flow rate and other parameters such as the fluid type, the structural setting and the nature of the hosting sediment, a variety of types of structures can be developed (Løseth *et al.* 2009).

Seismic technology is established as the key tool to study these fluid escape structures, thanks to its ability to provide high resolution 2-D and 3-D images of the subsurface. Fluid escape structures manifest themselves on seismic reflection data as vertical to subvertical columnar zones of distorted reflections, widely known as ‘chimney’ and ‘pipe’ structures (Andresen 2012; Cartwright & Santamarina 2015; Karstens & Berndt 2015). In the literature, these terms are used interchangeably and may also have been collectively termed acoustic pipe structures, blow out pipes, seismic chimneys and gas chimneys (Cartwright & Santamarina 2015). Hereafter, we use the term ‘chimney’ to cover all these features. Chimneys are frequently associated with brightened and/or blanked seismic reflections, indicating the presence of free gas, authigenic carbonate cementation, and/or gas hydrate (Berndt 2005; Cartwright *et al.* 2007; Løseth *et al.* 2009; Plaza-Faverola *et al.* 2010; Løseth *et al.* 2011).

Chimney structures can appear in various forms such as diffuse shadows/clouds, funnels and pipes with widths and heights of a few metres up to several kilometres (Løseth *et al.* 2009; Davies *et al.* 2012; Yarushina *et al.* 2021). They can occur in isolation (Arntsen *et al.* 2007) or in clusters (Karstens & Berndt 2015), distributed linearly along faults, structural or topographic highs, buried scarps, pinch outs (Moss & Cartwright 2010) or meandering buried channel sand bodies (Gay *et al.* 2006). Chimneys may undergo continuous or episodic flow activity (Løseth *et al.* 2011) with variable inactive periods, from hours to thousands of years (Leifer & Boles 2005). During the dormant periods, there is no direct evidence of active fluid flow; however the eruptive flow causes permanent changes to the sediment layering as well as the creation of pockmarks, which can be used as a proxy to find such structures during inactive periods (Løseth *et al.* 2009; Böttner *et al.* 2019). Pockmarks are seabed depressions that are formed above subsurface fluid escape structures when the flux is high and eruptive (Brown 1990; Räss *et al.* 2018). Pockmarks may be circular, elliptical or composite (i.e. merged pockmarks) in shape, and their diameters can range from a few metres up to several hundreds of metres, with depths up to several tens of metres relative to the surrounding seafloor (Hovland *et al.* 2002;

Gay *et al.* 2003; Andresen *et al.* 2008; Løseth *et al.* 2009; Cathles *et al.* 2010; Böttner *et al.* 2019; Andresen *et al.* 2021). Cathles *et al.* (2010) suggest that co-occurrence of rapid fluid discharge and strong seafloor currents can explain the generation of pockmarks.

The Scanner Pockmark complex, an active fluid escape structure in the North Sea, provides an analogue to possible CO<sub>2</sub> leakage scenarios in carbon capture and storage (CCS) sites (Robinson *et al.* 2021). Carbon isotope ratios of the seeping methane suggest a combination of microbial and thermogenic origins, with the Late Jurassic-lowermost Cretaceous Kimmeridge Clay and Tertiary age peats as possible source rocks (Clayton & Dando 1996; Judd & Hovland 2007). The gas migration system at the Scanner Pockmark complex has been investigated by several researchers using a variety of techniques (Robinson *et al.* 2021). Bayrakci *et al.* (2021) applied a shear wave splitting technique to PS-converted waves and characterized very shallow sediments (i.e. 4–5 m below sea floor) beneath the Scanner Pockmark as a fractured zone with fracture azimuths of 70° and 160° that could be possible gas conduits. Robinson *et al.* (2022) applied the same technique to the Scanner Pockmark OBS data set and observed spatially varying anisotropy with strength of ~1–4 per cent within the sediments down to a depth of 50 m below the seabed. They correlated the derived anisotropy with calculated *P*- and *S*-wave velocities and concluded that the existing anisotropy is related to syn- and post-depositional glaciomarine processes. Gehrman *et al.* (2021) integrated controlled source electromagnetic (CSEM) data with seismic reflection and core log data to constrain a resistivity model of the subsurface to about 200 mbsf in the Scanner Pockmark area. They used porosity and resistivity measurements from representative cores to calibrate Archie’s parameters and estimated an average porosity of ~50 per cent at the seafloor, decreasing to ~25 per cent at ~150 mbsf. Additionally, using an extended Archie’s relationship, Gehrman *et al.* (2021) estimated a free gas saturation of 34±14 per cent for a 30–40 m-thick gas pocket at about 50–90 mbsf beneath the pockmark. The top and bottom of the gas pocket were constrained by a coincident 2-D seismic reflection data with a vertical resolution of about 2.5 m (Gehrman *et al.* 2021). Callow *et al.* (2021) carried out a comprehensive integrated interpretation of high-resolution seismic reflection data to characterize the Scanner Pockmark complex within a regional geological framework. They determined the spatial distribution of subsurface gas accumulation and showed that the venting gas is fed from a reservoir in a shallow glacial outwash fan at 80 mbsf. They interpreted that this shallow reservoir is hydraulically connected to deeper strata. Böttner *et al.* (2019) showed that all actively venting pockmarks within the Witch Ground Basin (i.e. Scanner, Challenger, and Alkor pockmark) are associated with underlying chimney-like structures. Schramm *et al.* (2021) applied traveltimes tomography to a set of OBS seismic data and suggested that the internal structure of the underlying chimney can be divided into a shallow (i.e. <260 mbsf) gas-filled zone and a deeper high-velocity zone at the base of upper Aberdeen Ground Formation. However, their model has a relatively high traveltimes misfit of 8 ms and low resolution.

In this study, we investigate the underlying chimney of the Scanner Pockmark complex, using seismic tomography. Seismic velocity acts as a proxy for porosity, lithology (including clay content and cementation) and pore fluid content variations (Han *et al.* 1986; Avseth *et al.* 2005). Thus, it can provide indirect information about subsurface fluid flow processes. In addition, seismic velocity can be used to discriminate real chimney structures from image artefacts generated by acoustic blanking. Signal distortion within gas-charged sediments, caused by scattering and attenuation of incident

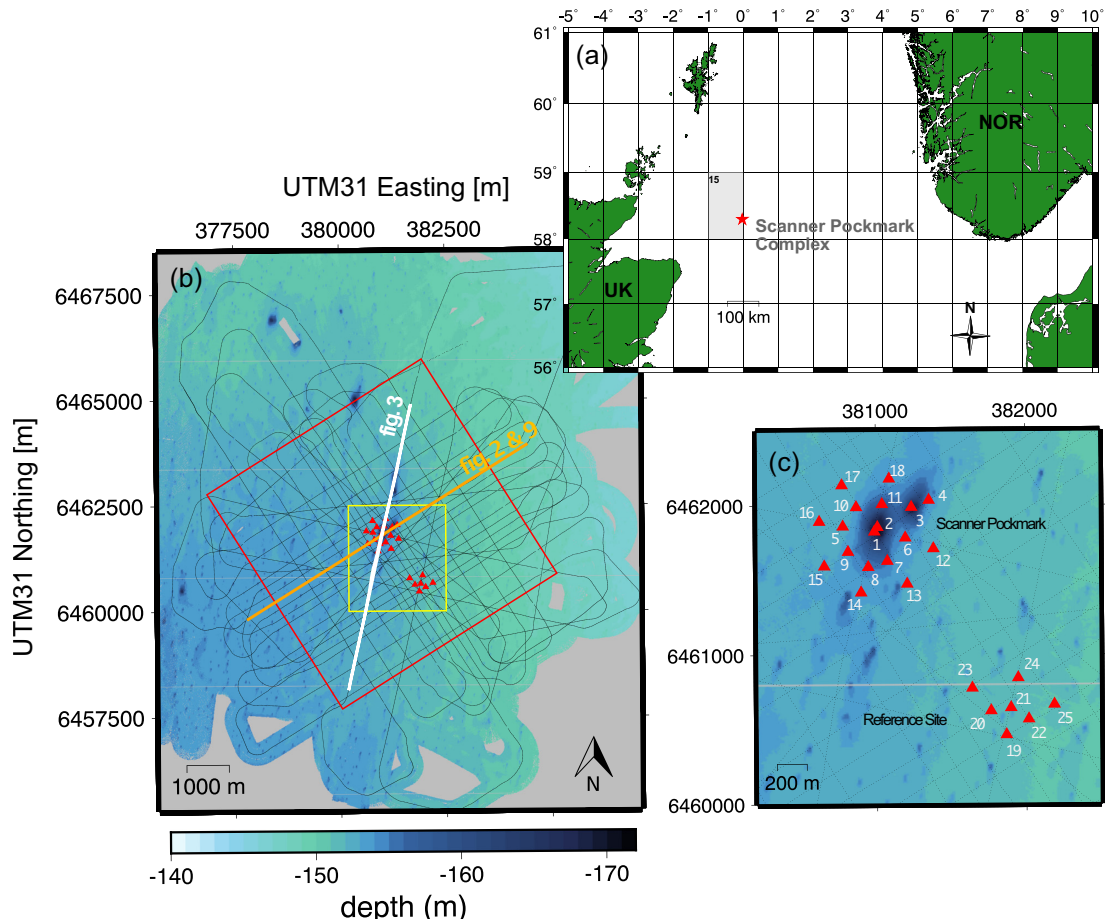


**Figure 1.** (a) Location of the Scanner Pockmark complex (red asterisks) in the North Sea. The Scanner Pockmark is located 190 km off the northeast coast of Scotland and situated within UK North Sea licence block 15/25. (b) Bathymetry of the Scanner Pockmark region with survey layout. The black lines mark GI gun acquisition tracks. The red solid triangles represent OBS positions. The yellow box shows borders of enlarged area shown in c and red box shows borders of inversion area. The orange line indicates location of profiles in Figs 2 and 9. The white line indicates location of profile shown in Fig. 3. (c) Enlarged area marked by yellow box in a. The red solid triangles mark OBS positions labelled by their numbers. Locations are shown in UTM zone 31 N.

energy, limits the imaging potential of reflection seismic data. In contrast, transmitted seismic energy allows for determination of velocity variations within fluid escape structures. We applied first arrival traveltome tomography to a densely sampled wide-azimuth and wide-angle OBS seismic data set acquired during RRS James Cook cruise JC152 (Bull 2018), similar to that used by Schramm *et al.* (2021). We were able to achieve much improved resolution compared to that of Schramm *et al.* (2021) by picking traveltimes with lower uncertainty, carrying out a more comprehensive statistical analysis, and following a different approach to define the starting model, all of which have a major influence on the inversion result.

## 2 GEOLOGICAL SETTING

The Scanner Pockmark complex (Fig. 1) is a methane gas venting seafloor depression located in the Witch Ground Basin, 190 km off the northeast coast of Scotland. Methane is vented at a rate of  $1.6\text{--}2.7 \times 10^6 \text{ kg yr}^{-1}$  (Li *et al.* 2020). The Scanner Pockmark complex comprises two overlapping seabed pockmarks with a combined size of about  $900 \text{ m} \times 450 \text{ m}$  wide and 22 m deep, lying in  $\sim 155 \text{ m}$  water depth (Fig. 1). Samples of methane-derived authigenic carbonate (MDAC) have been observed both on the seabed (Judd & Hovland 2007), and in cores retrieved from shallow drilling

(Robinson *et al.* 2021). MDAC is a common by-product of seeping methane, depositing within anaerobic intervals of seabed sediments. The Scanner Pockmark is underlain by a chimney-like structure (Fig. 2) that is hosted by a  $\sim 300 \text{ m}$ -thick Quaternary sediment succession and the underlying Neogene-age Nordland Group. The Nordland Group is predominantly claystone, interbedded by several sandstone and limestone layers (Judd *et al.* 1994). The top of the Nordland Group is characterized by a regional unconformity, the Crenulate Reflector (CR), on which seismic bright spots indicate the presence of gas-filled sand channels (Böttner *et al.* 2019; Callow *et al.* 2021). The basal unit of the Quaternary sediments, the Aberdeen Ground Formation (AbG Fm.), is composed of layered sands, silts and clay-rich sediments (Stoker *et al.* 2011) that represent a cap-rock (Böttner *et al.* 2019). The top of the Aberdeen Ground Fm. is characterized by an irregular regional glacial unconformity (Stewart & Lonergan 2011). The Aberdeen Ground Fm. is overlain by stacked glacial deposits including the Ling Bank Formation (LB Fm.), Coal Pit Formation (CP Fm.), Last Glacial Maximum deposits (LGM) and Witch Ground Formation (WG Fm.). The top of the Aberdeen Ground Fm. is eroded by several tunnel valley incisions (infilled subglacial channels) of the Ling Bank Fm. (Stewart & Lonergan 2011). The Ling Bank Fm. is comprised of two sub-units, namely, the basal unit (S2.1) composed of coarse sands and gravels and the upper unit (S2.2) that is interpreted as outwash

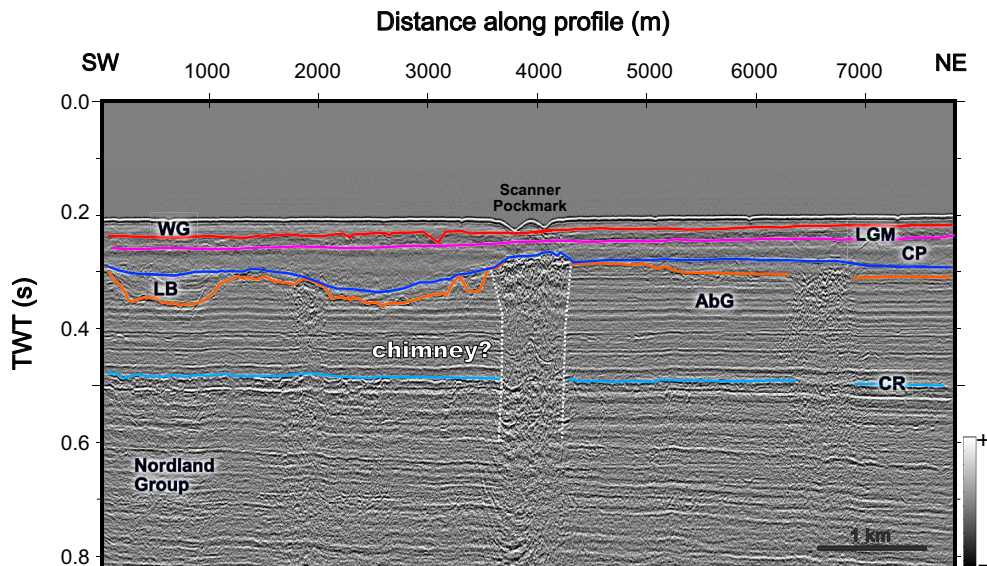


**Figure 2.** Seismic reflection section from the Scanner Pockmark region showing interpreted stratigraphic features. The seismic profile is oriented SW to NE across the Scanner Pockmark complex, indicated by the orange line in Fig. 1(b). Tops of interpreted stratigraphic units are shown with coloured lines. Formations are labelled by their abbreviations: CR—Crenulate Reflector, AbG—Aberdeen Ground Fm., LB—Ling Bank Fm., CP—Coal Pit Fm., LGM—Last Glacial Maximum deposits, WG—Witch Ground Fm. The chimney outline is displayed with two subvertical white dotted lines. TWT stands for Two-Way Traveltime.

channels and is composed of clay-rich sediments (S2.2-ii) and gas-filled coarse sands (S2.2-iii) (Stoker *et al.* 2011; Callow *et al.* 2021). West of the Scanner Pockmark, a ~1 km wide tunnel valley is oriented SE–NW. The tunnel valley is over 100 m deep and is overlain by the 10–30 m-thick gas-filled S2.2-iii unit (Callow *et al.* 2021). In addition, a ~1 km-wide E–W outwash channel of the S2.2 unit lies east of the Scanner Pockmark. Brightened seismic reflection patches with reversed polarity are observed at structural highs of the S2.2 unit between adjacent valleys (Böttner *et al.* 2019), suggesting the presence of gas-bearing sediments. The Coal Pit Fm., overlying the Ling Bank and Aberdeen Ground Fm., comprises glacial tills with dark to brownish grey, muddy and pebbly sands or sandy muds (Graham *et al.* 2010; Stoker *et al.* 2011). The seismic character of the Coal Pit Fm. and the subunit S2.2 of the Ling Bank Fm. are similar and indistinguishable in some areas (Callow *et al.* 2021). The shallowest formation is the Witch Ground Fm., which consists of finely laminated glaciomarine sediments (Stoker *et al.* 2011).

### 3 TOMOGRAPHY METHOD

In this study, the 3-D First Arrival Seismic Tomography (FAST) code of Zelt & Barton (1998) is used. FAST is a regularized tomographic method in which the simplest model is sought that minimizes first-arrival traveltime residuals down to their assigned uncertainties (Zelt *et al.* 2006). The model and ray paths are iteratively updated until the normalized squared-misfit criterion, eq. (1), is satisfied.

$$\chi^2 = \frac{1}{N} \sum_{i=1}^N \left( \frac{t_i^o - t_i^p}{\sigma_i} \right)^2 = 1 \quad (1)$$

where  $N$  is the number of data points,  $t_i^o$  and  $t_i^p$  are the  $i$ th observed and predicted traveltime, and  $\sigma_i$  is the assigned  $i$ th traveltime pick uncertainty.

Forward calculations of traveltimes and ray paths are based on a modified version of Vidale's method (Hole & Zelt 1995), in which

the eikonal equation is solved using a finite-difference scheme. Inversion is formulated as a minimization of an objective function. The objective function in FAST is defined as a least-squares norm including the traveltime errors and two additive regularization terms to constrain the model perturbation and the smoothness level of the inverted model (see eq. 2 below; Zelt & Barton 1998).

$$\Phi(s) = \delta t^T C_d^{-1} \delta t + \lambda [\alpha (S^T W_h^T W_h S + s_z S^T W_v^T W_v S) + (1 - \alpha) \delta S^T W_p^T W_p \delta S]. \quad (2)$$

In eq. (2),  $\Phi$  denotes the objective function,  $\delta t$  is the traveltime misfit vector,  $S$  is the model slowness vector,  $\delta S$  is the perturbed model vector,  $C_d$  is the data covariance matrix that contains the estimated pick uncertainties,  $W_p$  is the perturbation weighting matrix (i.e. a diagonal matrix containing the reciprocal of the starting slowness values), and  $W_h$  and  $W_v$  are the horizontal and vertical roughness matrices (i.e. second-order spatial finite-difference operators), respectively. The value  $s_z$  controls the relative weight of the vertical and horizontal smoothing regularization. Trade-off between the smallest perturbation versus smoothness constraints can be adjusted via the parameter  $\alpha$ .  $\lambda$  is a trade-off parameter between data and the model terms in the objective function and determines the overall amount of regularization. For further details, the reader is referred to Zelt & Barton (1998).

### 4 DATA ACQUISITION AND PRE-PROCESSING

#### 4.1 The CHIMNEY seismic experiment

In 2017, the CHIMNEY seismic experiment was carried out to investigate the Scanner Pockmark complex, located in the central North Sea (Bull 2018). During the cruise, a GI gun seismic source was shot into a grid of 25 OBS arranged over the Scanner Pockmark complex (Fig. 1). The GI gun source array comprised two 105 cu. in. chambers that were towed at 2 m below the sea surface and

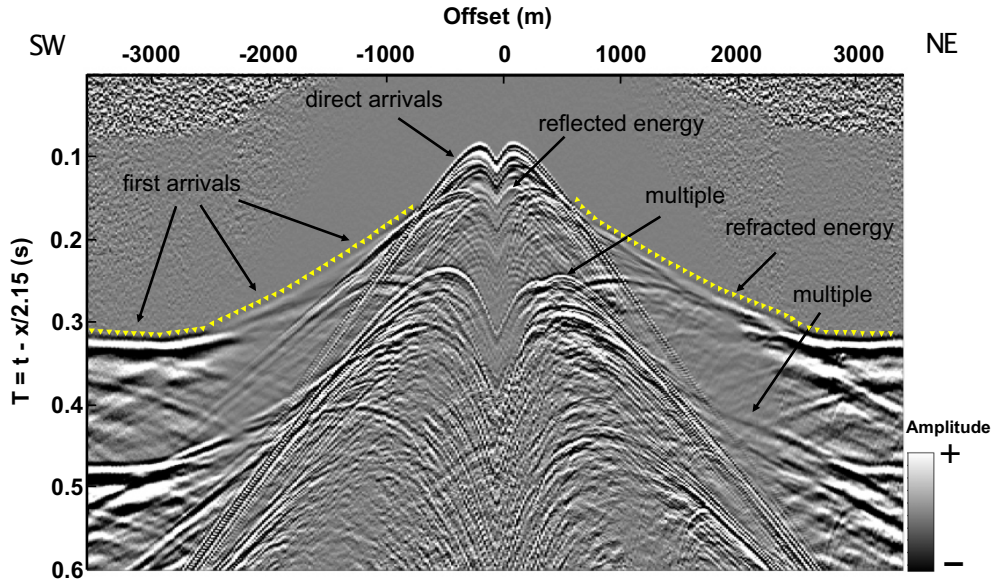


**Figure 3.** Vertical component of the GI-gun data from OBS-8 for the profile highlighted in Fig. 1(b). A bandpass filter of 10–30–350–400 Hz and a reduction velocity of  $2.15 \text{ km}^{-1}$  have been applied. The amplitude is boosted by automatic gain control with an operator length of 0.5 s. The yellow triangles mark first arrival traveltimes corresponding to refracted waves.

fired at 8 s intervals. This source provided a 5–300 Hz bandwidth at  $-20 \text{ dB}$ , and a reasonable balance between data resolution and penetration depth. The ship’s speed was  $\sim 4.5 \text{ kn}$ , resulting in an average shot spacing of  $\sim 18.5 \text{ m}$ . Eighteen OBSs were deployed within and around the pockmark and seven were deployed at a reference site located  $\sim 1 \text{ km}$  southeast of the Scanner Pockmark where no gas or seismic chimney is observed to be present in the subsurface (Robinson *et al.* 2021). The OBS spacing within these arrays varies between 20 and 200 m. Shot lines were designed as asterisk and grid survey geometries in order to enhance azimuthal coverage and regular sampling of the subsurface, respectively. The OBS sampling interval was 0.25 ms. Clock drifts were corrected by assuming a linear drift between timing synchronizations immediately before deployment and after recovery. In this study, only the vertical geophone component data are used to invert the acoustic velocity model.

#### 4.2 Data QC: position and timing correction

We used an iterative data-fitting approach to jointly correct for uncertain OBS and shot positions and residual OBS clock timing errors. Direct arrivals were picked to maximum offset of 500 m, where refracted arrivals become first arrivals. Time picks were fitted to the simulated first arrival times calculated using traveltime equation (eq. 3).

$$T^2 = T_o^2 + X^2/V_w^2, \quad T_o = (Z_r - Z_s)/V_w, \quad (3)$$

where  $T$  and  $T_o$  are total traveltime and vertical traveltime respectively,  $Z_r$  is receiver depth,  $Z_s$  is shot depth,  $V_w$  is water velocity and  $X$  is the horizontal offset. The observed and calculated direct arrival times were minimized in a least-squares sense by updating shot and receiver locations and timing ( $\tau_s$  &  $\tau_r$ ). Although shot times were known, we updated the source timing throughout the process as a proxy for the overall effect of gun depth, tides and wave height variations. We found that this approach was more robust in contrast to correcting for both the water depth (due to tides

and waves) and source depth variations. Additionally, to simplify the analysis, we assumed a constant time and position error for each sail line (i.e. equivalent to allowing for feathering of the towed GI gun array). In the first step,  $X_r$  (receiver x-coordinate),  $Y_r$  (receiver y-coordinate) and  $\tau_r$  (receiver timing) were determined followed by updating  $X_s$  (source x-coordinate),  $Y_s$  (source y-coordinate) and  $\tau_s$  (shot timing) values on a coarse grids. Then the process was iterated using a finer grid until the updated positions and timing reduced the direct arrival time residuals down to an acceptable error margin, that is root-mean-square (RMS) value of  $< 0.5 \text{ ms}$  with maximum residuals less than  $\pm 3 \text{ ms}$ . The water velocity was also allowed to vary throughout the iterations, but it was found that the velocity of  $1490 \text{ ms}^{-1}$  that was derived by a moveout analysis of the first arrivals is a good estimate.

#### 4.3 Traveltime picking

The seismic data were only corrected for any DC component and the first arrivals were picked manually at onset of refracted first arrivals of unfiltered seismic traces (Fig. 3). In order to avoid turns between acquisition tracks, which have low positioning accuracy, we confined our study into an area of  $6 \times 6 \text{ km}^2$  with its centre at OBS-1 and sides parallel to grid survey lines (i.e. rotated  $32^\circ$  clockwise from north). In total, 182 069 first-arrival traveltime picks from 24 OBSs were used for the inversion. OBS-17 was not used as the vertical component direct arrivals appeared to show asymmetric polarity change. We speculate that this is due to a tilted geophone sensor package, causing horizontal energy to leak onto the vertical component.

#### 4.4 Data uncertainty assessment

The inversion algorithm that is used in this study uses the normalized chi-squared (eq. 1) to assess the model updates, thus the 68 per cent confidence interval (i.e.  $\mu \pm \delta$ —where  $\mu$  is mean and  $\delta$  is standard deviation) of the residuals defines the uncertainty level.

We applied cross-over analysis to the traveltimes picks (Appendix A) and found an RMS cross-over error of  $\sim 3.5$  ms for our data. Thus a conventional approach would involve stopping inversions at a misfit of 3.5 ms. However, numerous runs showed that at 3.5 ms uncertainty level, final residual mean substantially deviates from zero at mid-far offsets. Additionally, several test runs showed that the inversion converges down to  $\sim 2$  ms RMS error with final residuals that have a mean close to zero at all offsets. This issue arises because pick errors are not independent, but are correlated from trace to trace, as documented by a Runs Test. The Runs Test is a statistical hypothesis test for detecting non-randomness. It randomly selects a sequence of residuals and examines their signs. Many repeating signs in a row implies non-randomness (Constable *et al.* 2015). Additionally, we carried out a synthetic test based on our real problem's characteristics (Appendix B) and investigated the effect of overestimating the data errors. Stopping at a misfit level that is too large resulted in large variations of the mean misfit at far-offset region (Fig. B1b), as seen with our inversions of real data. Thus, we chose 2 ms as the optimum data uncertainty level.

## 5 MODEL PARAMETRIZATION

In FAST, the model is parametrized by slowness grids. The inverse grid is cell-based but the forward grid is defined by nodes. We set a constant node spacing of 10 m along all directions for the forward traveltimes modelling step. The maximum forward node spacing must be defined such that the largest traveltimes modelling error remains below the assigned minimum traveltimes pick uncertainty. Thus, the maximum node spacing must satisfy the following inequality:

$$\delta t_{\max}^m \leq \delta t_{\min}^d; \delta t_{\max}^m = \left( \frac{(\sqrt{2} - 1) d_{\max}}{v_{\min}} \right), \quad (4)$$

where  $\delta t_{\max}^m$  is maximum modelling traveltimes error,  $\delta t_{\min}^d$  is minimum estimated data traveltimes error (i.e. data uncertainty),  $d_{\max}$  is maximum node spacing size, and  $v_{\min}$  is minimum velocity in the model. Assuming a minimum velocity of  $1490 \text{ ms}^{-1}$  (the water column velocity), the maximum node spacing that keeps the model error below the minimum traveltimes uncertainty of 2 ms is  $\sim 7$  m. However, we set the node spacing equal to 10 m to reduce the computational cost of forward modelling by a factor of  $\sim 3$  (i.e.  $10^3/7^3$ ) throughout the Monte-Carlo simulation runs. Qualitative inspection of the synthetic test results (Appendix B) showed that the larger node spacing, that is 10 m, can still result in acceptable inverted model, partly because the majority of ray paths penetrated cells that have a higher velocity than the water column. The velocity model covers an area of  $6 \times 6 \text{ km}^2$  down to a depth of 2 km and has  $72 \times 10^6$  nodes. The inverse model is parametrized as a uniform 100-m grid of slowness cells. The cell size is chosen to balance the trade-off between the resolution and the constraint on the inverted velocity values (Zelt *et al.* 2006). Smaller cells increase the inversion resolution, but can result in geologically unreasonable velocity variations.

## 6 INVERSION STRATEGY

Linearized inversions such as FAST require a representative starting model from which the inversion converges to the true model (van der Hilst & Spakman 1989; Kissling *et al.* 1994). We built the starting model using a heuristic approach in three steps. In the

**Table 1.** Mean ( $\mu$ ) and standard deviation ( $\sigma$ ) values assigned to the 1-D model's depths of layer boundaries and the velocities at those boundaries.

Depth	$\mu_{\text{depth}}$	150	250	400	600	800	2000
(mbsl)	$\sigma_{\text{depth}}$	0.01	15	25	30	35	55
Velocity	$\mu_{\text{velocity}}$	1600	1815	1890	2095	2250	3000
( $\text{m s}^{-1}$ )	$\sigma_{\text{velocity}}$	50	70	80	120	150	250

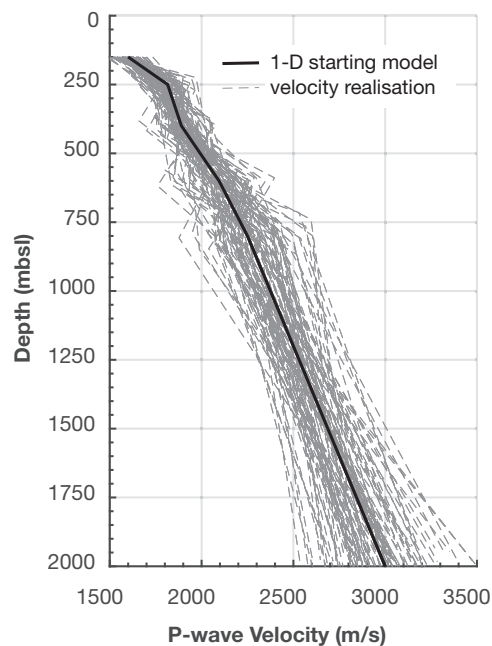


**Figure 4.** Monte Carlo velocity realizations. The solid black line marks the 1-D starting model and dashed lines show 100 randomly generated realizations.

first step, via a trial and error approach, we sought a 1-D layered starting model (laterally invariant plane layers with velocity increasing linearly with depth) that resulted in reasonably low initial residuals along all offsets for all OBS instruments. The seafloor was also added and the water column velocity fixed to  $1490 \text{ ms}^{-1}$  throughout the inversion. The resulting 3-D inverted model using this 1-D starting model led to an unsatisfactory final residual distribution, with the mean varying significantly with offset. Next we used a Monte-Carlo simulation to test alternative plausible starting models and to quantify the uncertainty of the inverted model. To this end, the original 1-D model was perturbed using normally distributed values for the depths of layer boundaries and the velocities at those boundaries (Table 1). The standard deviation was required to increase with depth. In total, 100 1-D model realizations were sampled randomly (Fig. 4) and inverted in 3-D, assuming a data uncertainty of 4 ms (from the cross-over analysis) and parameters  $\alpha$  and  $s_z$  equal to 0.5 and 0.1, respectively. 95 per cent of the inverted models had a normalized chi-squared of  $\sim 1$  (at 4 ms uncertainty level), but the corresponding residuals still showed large variations in mean value with offset, supporting the existence of correlated error in the picks. Finally, the inverted 3-D models with normalized chi-squared of  $\sim 1$  were averaged. The 3-D average model returned initial RMS traveltimes residual and normalized chi-squared values equal to 7.8 ms and 3.8, respectively. We applied a linear depth-variant scaling to the 3-D average model (Appendix C) to correct for the nearly linear bias in the residuals (Fig. C1a), such that the residuals oscillate around the mean value of zero. The scaled 3-D

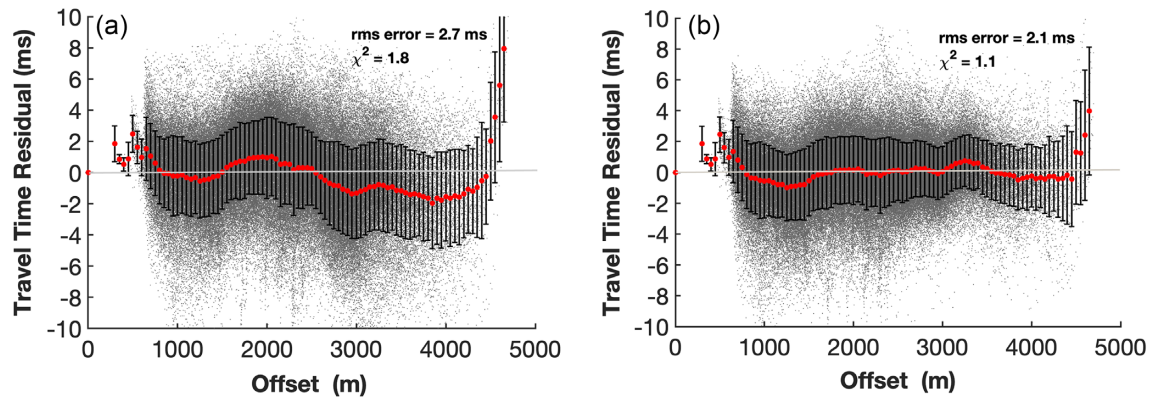


**Figure 5.** (a) Initial data residuals for the 3-D starting model as a function of source–receiver offset. The grey dots show individual residuals. The red dots show averaged residuals and vertical black lines show error bars (68 per cent confidence limit) for residuals within every 50-m offset bin. (b) Final data residuals after three iterations.

averaged model had initial RMS error and normalized chi-squared of 2.7 ms and 0.46, respectively (Fig. C1b). For subsequent inversions we used the scaled 3-D average model as the starting model, hereafter referred to as the 3-D starting model.

For our final inversion run, the free parameters  $\alpha$  and  $s_z$  were set to 0.9 and 0.1, respectively (see Appendix D for more details) and the data uncertainty is set to 2 ms, as discussed in subsection 4.4. After preliminary inversion runs, we visually inspected picks with large final residuals ( $> 12$  ms). It appeared that they fall randomly in farthest offset regions where the data signal-to-noise ratio is low and picks are prone to large uncertainty. For further inversions, we cleaned the data by removing these erroneous picks that were about 1.4 per cent of the total picks. After three iterations, initial RMS traveltimes residual and normalized chi-squared values reduced from 2.7 ms and 1.8 (using 2 ms uncertainty level; corresponding to 2.7 ms and 0.46 at 4 ms uncertainty level) respectively to 2.1 ms and 1.1 (Fig. 5).

## 7 MODEL RESOLUTION

Checkerboard testing was applied in order to determine the spatial resolution of the final inverted model (Zelt & Barton 1998). Alternating velocity perturbations of  $\pm 5$  per cent were introduced to the 3-D starting model, with tests performed for three checkerboard anomaly sizes of 200, 500 and 1000 m. The inversion resolution was evaluated using the same source–receiver geometry used as that for the real inversion. The recovered checkerboard anomaly patterns are displayed in Fig. 6.

Our testing shows that uniform anomalies with 200 m, 500 m and 1 km size can be resolved down to 200, 400 and 600 mbsl, respectively, where the inversion cell ray hit-count is  $> 100$ . These anomaly sizes can be further interpreted down to 300, 500 and 700 mbsl, respectively, where the inversion cell ray hit-count is  $> 500$ . Within the inverted model (Fig. 7), ray paths are concentrated below the Scanner Pockmark and the reference site (where the OBS instruments are deployed) and across the depth interval between the seabed and the Crenulate Reflector ( $\sim 150$ – $500$  mbsl) (Fig. 8). Ray path concentration drops sharply away from the OBS locations and displays a strong correlation with survey track lines. This leads to the presence of an acquisition imprint at shallow depths in the inverted model that partially obscures the geometry of the anomalies (Fig. 8a, map 200 mbsl). However, a number of structures can be robustly detected, and are discussed below.

## 8 RESULTS

In our final model, the velocity ranges between 1600 and 2200  $\text{ms}^{-1}$  across a 550 m depth interval below the seabed (Fig. 7). The velocity anomaly ranges from  $-125$  to  $+110$   $\text{ms}^{-1}$  relative to its average 1-D model (Fig. 8). In the first 100 m below the seabed (Fig. 8a, 200-mbsl map, including the WG, LGM, CP and LB Fm.) a high-velocity zone (in blue) dominates the area bounded by the 100 hit-count contour line. This high velocity zone is breached by several low velocity structures including a  $\sim 0.2 \times 2$  km NW–SE channel-like low-velocity structure (labelled Ch) that approaches to the pockmark at its SE end. A low velocity zone is also evident below the Scanner Pockmark location. In addition, an approximately  $3.5 \times 1$  km NW–SE low-velocity anomaly (labelled TV) is observed towards the SSW of the pockmark. The dominating high-velocity anomaly structure extends down to 300-mbsl (including LB and AbG Fm.) to the NNE of the pockmark (labelled H on 200- and 300-mbsl maps of Fig. 8a). In the 300-mbsl depth slice in Fig. 8(a), the inverted model shows a high velocity anomaly beneath the Scanner Pockmark, suggesting the presence of an impermeable layer across the observed chimney structure in the seismic reflection image. In the 400-mbsl depth slice of Fig. 8(a) (including the AbG Fm. and part of the Nordland Group), a low velocity anomaly expands in the form of an ellipse (labelled G) with minor and major axis lengths of about 2 and 3 km, respectively. Next to the pockmark towards the west, the anomaly shows an evident amplitude increase of around  $-100$   $\text{ms}^{-1}$  (denoted by a black arrow on the 400-mbsl depth slice in Fig. 8a) that stands out from the rest of the anomaly. In the 500-mbsl map (including the Nordland Group), a  $\sim 500$  m  $\times$  300 m low-velocity anomaly is evident at the pockmark location (labelled P1) that is embedded within a high velocity anomaly ring with the outer diameter of  $\sim 1.2$  km. As demonstrated in the synthetic test (Appendix B), this high velocity ring can be an artefact (compare 500-mbsl maps in Figs B2a and b). The P1 low velocity anomaly extends down and appears on the 600-mbsl map, shifted  $\sim 400$  m towards the north. Two noticeable features at 500-mbsl are the sharp boundaries between high and low velocity zones (marked by cyan dashed lines in Fig. 8a). As the depth increases down to 700 mbsl, only anomaly structures with dimensions  $> 1$  km can be interpreted within the regions where hit-counts are 500 per cell. An example anomaly is a low velocity structure appearing towards the SE of the pockmark on 600- and 700-mbsl depth slices (labelled P2 in Fig. 8) that is surrounded by a circular high velocity anomaly with about 3.5 km diameter.

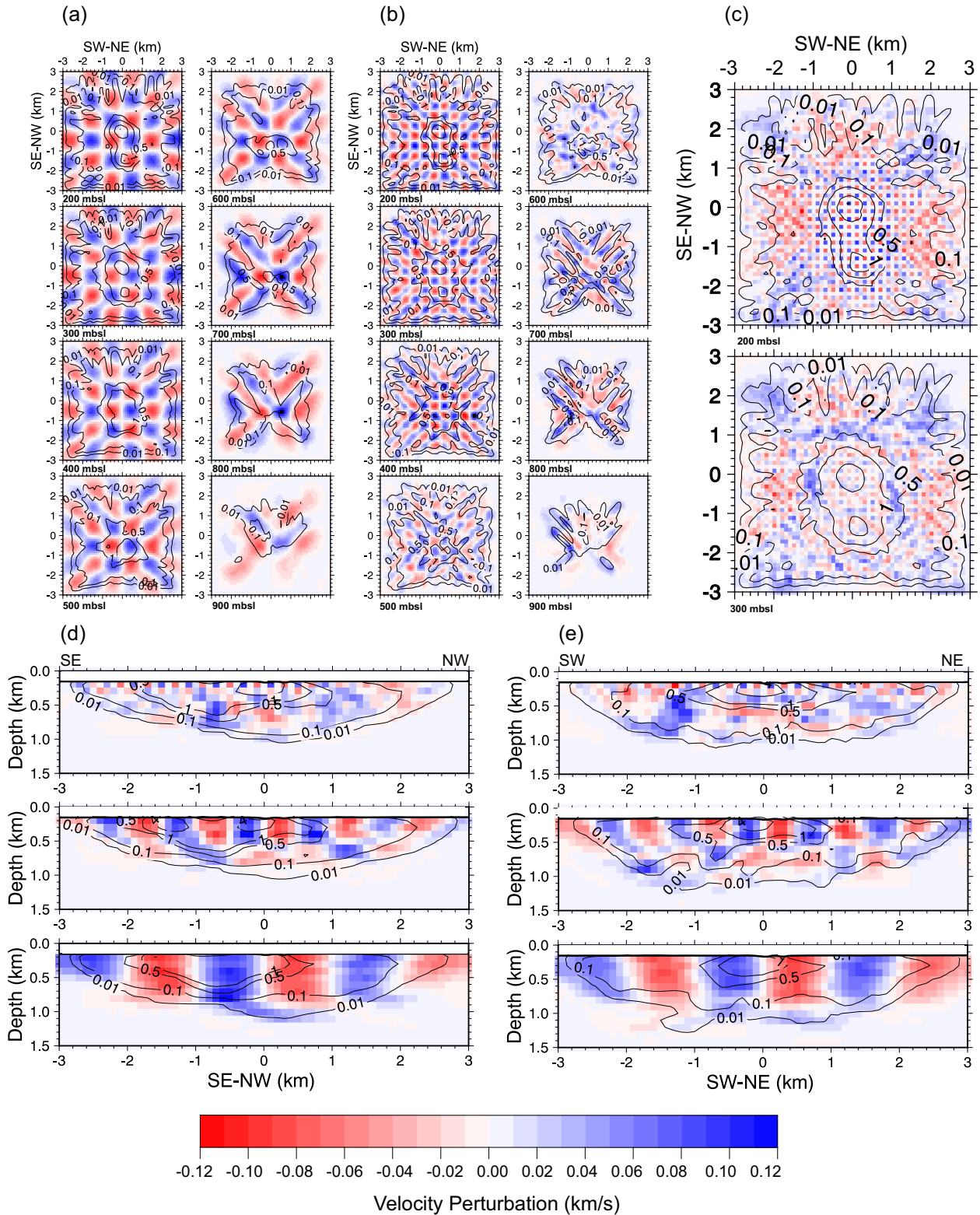


**Figure 6.** (a)–(c) Recovered checkerboard anomaly pattern maps for uniform 1000-m, 500-m and 200-m anomaly sizes, respectively. Panel (c) shows only the first two depth-slices of 200 and 300 mbsl where tomography could resolve parts of anomalies with 200-m size (beyond which, 200-m anomaly size has not been recovered). Recovered checkerboard anomaly pattern on SE–NW section (d) and SW–NE section (e) of 1000-m (bottom row), 500-m (middle row), 200-m (top row) anomaly sizes passing through middle of anomaly blocks placed next to the Scanner Pockmark. The red and blue colour denote low and high velocity anomalies, respectively. Scanner Pockmark is located at the middle of the maps at co-ordinates (0, 0). The solid black lines show hit-count contour lines (annotations are in  $10^3$ ).

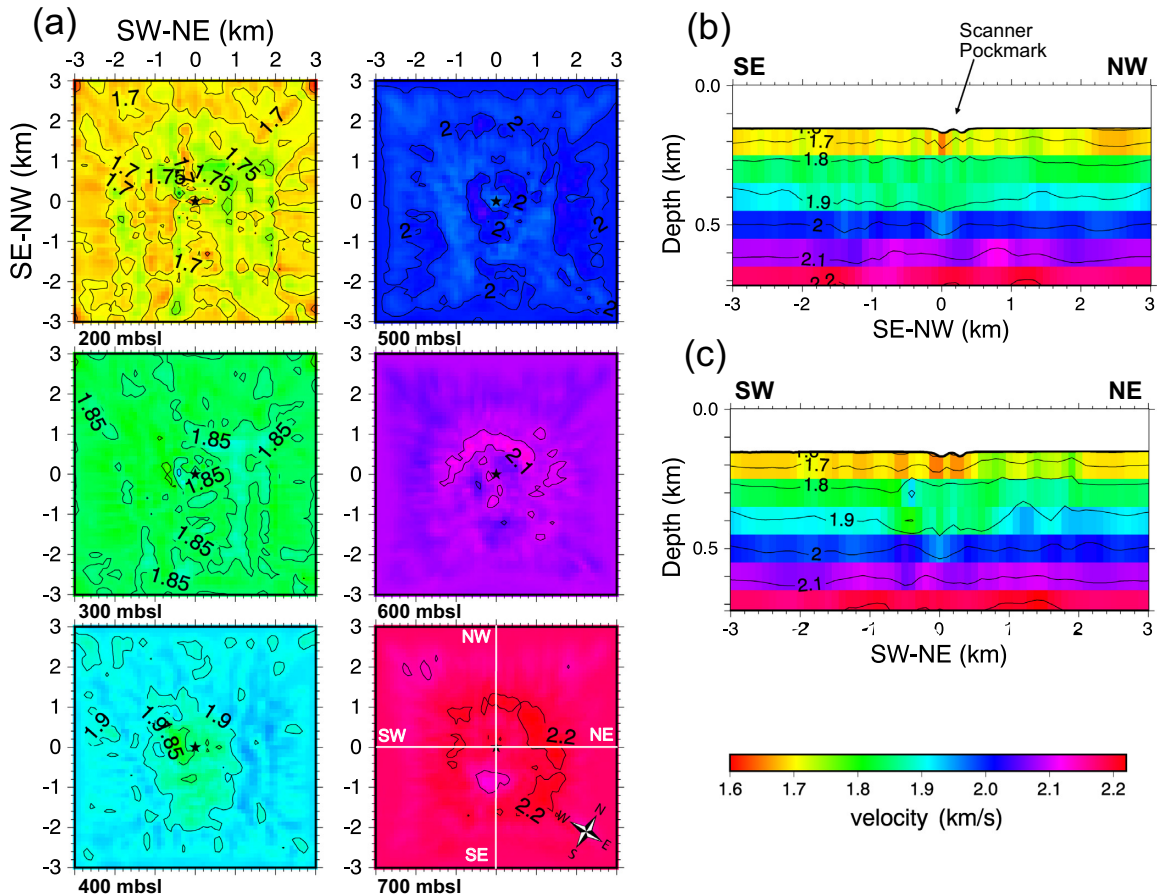


**Figure 7.** Tomographic velocity model of the subsurface at the Scanner Pockmark complex area. (a) Absolute velocity depth-slice maps at 100 m depth intervals from 200 to 700 m depth below sea level. (b) and (c) display SE–NW and SW–NE absolute velocity cross sections, respectively, down to 700 mbsl depth. White lines on 700-mbsl map mark the cross sections locations. The solid black lines show the velocity contour lines in  $\text{km s}^{-1}$ . Scanner Pockmark is located at middle of the maps at co-ordinates (0, 0) and is indicated by a black asterisk.

## 9 DISCUSSION

### 9.1 Correlation with multichannel seismic data

In general, despite the inherent resolution difference between the two methods ( $\sim 5$ – $10$  m vertical resolution and  $\sim 30$ – $45$  m horizontal resolution of the 3-D reflection seismic data (Callow *et al.* 2021) compared to  $>100$  m resolution of the tomographic model, there is good agreement between the multichannel seismic image and the inverted model within the well resolved regions (Fig. 9a). A simplified schematic of the interpreted gas migration path across the seismic reflection image is displayed in Fig. 9(b). The latter figure also highlights the difference between the inversion cell height and the stratigraphic unit thicknesses in the region. Beneath the Scanner Pockmark, coincidence of inverted low velocity anomalies with distorted and brightened reflections of the Ling Bank Fm. ( $\sim 260$  ms TWT in Fig. 9a—brightened reflections are evident in Fig. 2) and the Crenulate Reflector ( $\sim 500$  ms TWT in Fig. 9a) indicates that the observed chimney-like anomaly on the seismic reflection profile (indicated by dotted cyan lines and labelled A in Fig. 9a) represents a genuine complex fluid escape structure. Nevertheless, the distorted signals are related to both real fluid escape structures and associated artefacts that are distinguishable with the aid of our velocity model—gas-bearing sediments are linked to the low-velocity anomalies. We find that the chimney-like signal seen within the Aberdeen Ground Fm. (Fig. 9a,  $\sim 260$ – $500$  ms TWT)

overlaps a high-velocity anomaly and is indeed an artefact generated by the overlying Ling Bank Fm. gas pockets at about 260 ms TWT. This is consistent with the interpretation of Böttner *et al.* (2019) in which they suggested that the Aberdeen Ground Fm. acts as an impermeable cap rock.

The seismic reflection data also show two other chimney-like structures, indicated by dotted cyan lines and labelled B and C in Fig. 9(a). Neither of these chimney-like structures coincide with low velocity anomalies, and they are situated on the edge or outside the well-resolved areas (defined by ray hit-count of  $>100$  in Fig. 9a). Below anomaly B we observe deformed reflections, indicated by the red arrows in Fig. 9(a), suggestive of vertical fluid flow. However, above these reflections, at  $\sim 400$  ms TWT, we observe a seemingly intact overlying reflection, while the velocity anomaly across the distorted signals reaches up to  $+20$   $\text{ms}^{-1}$ , leaving interpretation of this feature uncertain.

Comparison of the maximum reflection amplitude extracted over the unit S2.2 interval of the Ling Bank Fm. with our velocity anomaly map at 200 mbsl (Fig. 10) shows that there is a correlation between the high reflection amplitudes and low seismic velocity channel-like feature aligned along SE–NW (indicated by a cyan oval in Fig. 10), indicative of the presence of gas. The channel reaches the pockmark at its SE end (indicated by the solid cyan line in Fig. 10). This channel at its NW end bends towards the NNE and connects to the shallow reservoirs of the Ling Bank Fm.

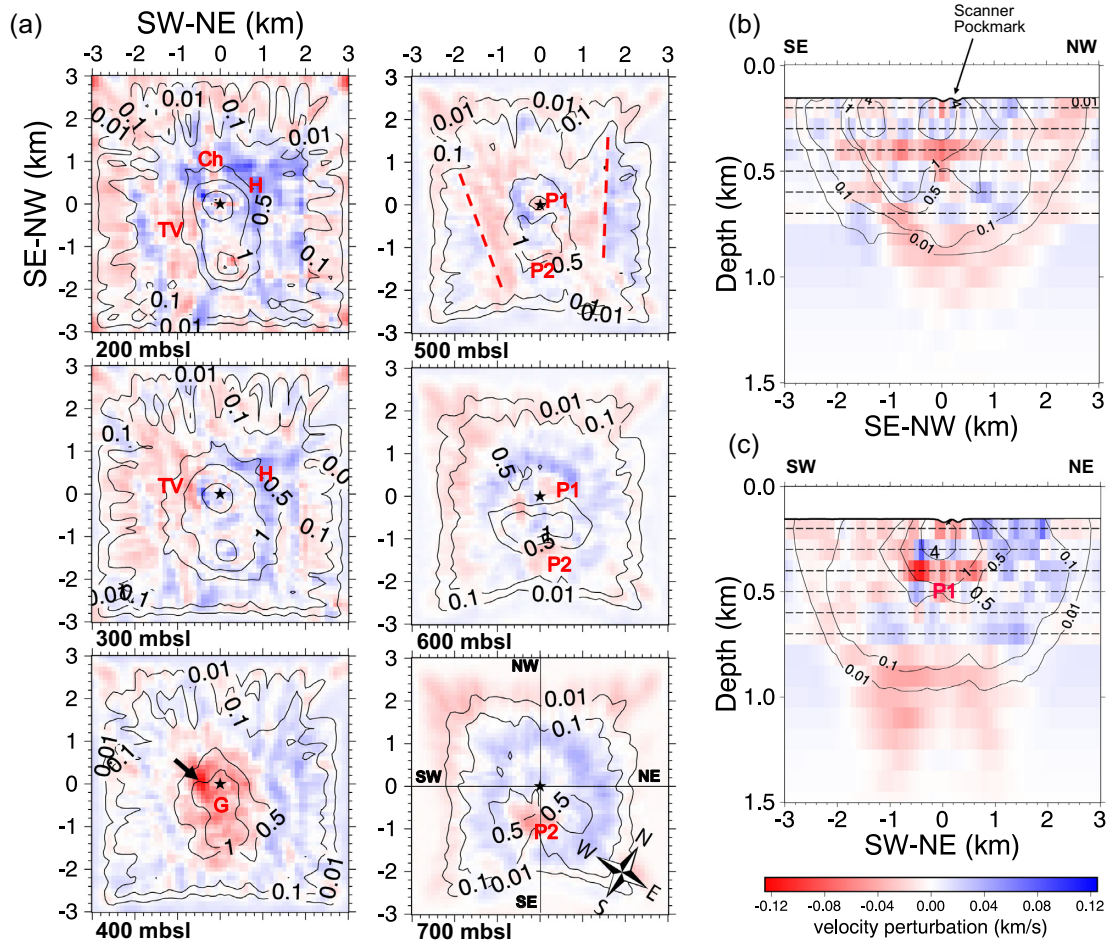


**Figure 8.** Map view (a) and cross sections (b, c) of inverted velocity anomaly structures (the difference between inverted model and its average 1-D model). Map views showing inverted anomaly structures at 100 m depth intervals from 200 to 700 m depth below sea level. The red and blue colour denote low and high velocity zones, respectively. The SW–NE and SE–NW cross sections passing through Scanner Pockmark in the middle of the model are denoted by solid black lines on 700-mbsl map. The dashed black lines in (b) and (c) indicate depths of anomaly maps shown in (a). The solid black lines show hit-count contour lines (annotations are in  $10^3$ ). Scanner Pockmark is located at middle of the maps at co-ordinates (0, 0) and is indicated by black asterisk. Ch, TV, G, H, P1 and P2 on the map views denote anomaly structures discussed in the text. The black arrow on 400 mbsl map shows location of an increased low velocity anomaly that could be possible vertical migration pathway from CR to the shallower strata. The dashed red lines on 500-mbsl map show fault line like features in the inverted model.

discussed by Callow *et al.* (2021). This feature suggests a potential horizontal fluid migration path. The comparison also shows that the SE–NW tunnel valley, delineate by the two dashed cyan lines in Fig. 10, is characterized by a negative velocity anomaly with an amplitude similar to that of the gas-filled SE–NW channel. However, the reflection amplitude map shows weaker amplitude compared to the one along the SE–NW channel structure. The negative velocity anomaly might be caused by the presence of thin gas-charged layers in the Ling Bank Fm. within the tunnel valley, which appears dimmed on seismic reflection data due to destructive interference. Alternatively, it may indicate that the tunnel valley is acting as a conduit allowing gas migration from deeper strata to shallow depths, leading to similar acoustic impedance across the reflectors, thus dimming the reflection amplitude rather than generating high amplitude anomaly. There is no evidence for either of these interpretations in seismic reflection data. The dashed cyan lines in Fig. 10 are picked along two narrowly elongated high velocity features on the velocity anomaly map that follow the rims of the SE–NW tunnel valley, suggesting compaction of sediments during creation of the incised valley. While these elongated features

cross-cut the acquisition lines, the other high velocity lineaments towards the east of the Scanner Pockmark lie between acquisition lines and appear to be acquisition imprint artefacts.

The rather sharp boundaries separating high and low velocity zones at 500 mbsl (within the Nordland Group) in Fig. 8(a) (marked by two dashed red lines) resemble fault lines. These features are located at  $\sim 2500$  and  $\sim 5500$  m distance along the seismic reflection profile at about 600 ms TWT in Fig. 9. The seismic reflection profile suggests presence of faults with small throw (a few tens of milliseconds TWT) at and below the CR horizon; however, we could not identify a clear correlation between the fault-like features in the inverted model and the reflection seismic data.

## 9.2 Gas saturation

In sediments with porosity greater than critical porosity (i.e. the porosity above which sediments are in suspension state), seismic velocity is fairly insensitive to porosity variation (Nur *et al.* 1998). The average porosity of the sediments overlying the Aberdeen Ground Fm. is  $\sim 40$  per cent (Gehrmann *et al.* 2021), equal to the critical

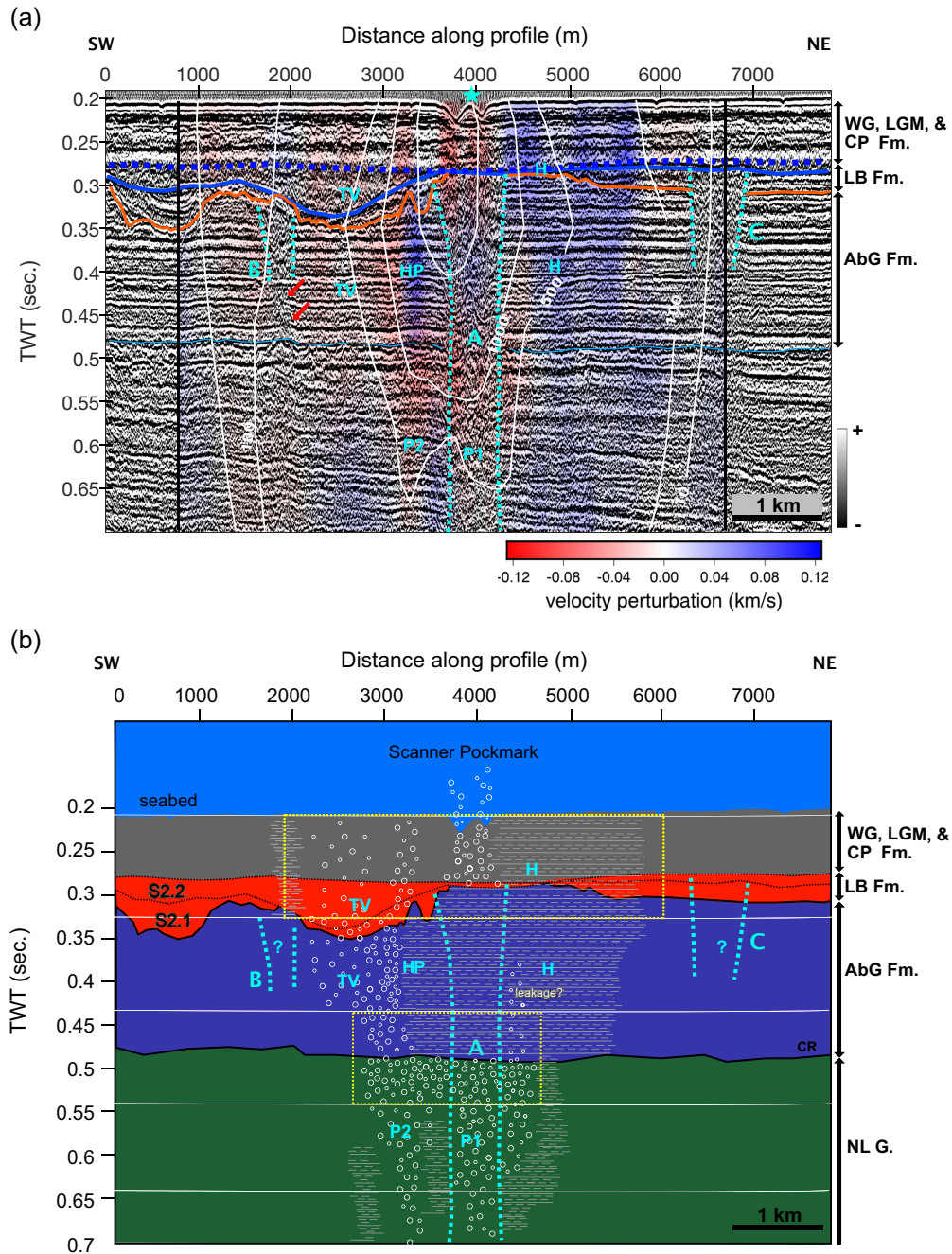


**Figure 9.** (a) Velocity anomaly profile in the time domain superimposed on a corresponding SW-NE seismic reflection profile crossing the Scanner Pockmark marked by the cyan star. The solid dark blue line shows top of the subunit S2.1 of the Ling Bank Fm., dotted blue line shows approximate top of the subunit S2.2 of the Ling Bank Fm. (the subunit S2.2 and the overlying CP Fm. have similar seismic character), orange line shows top of the Aberdeen Ground Fm., and light blue shows Crenulate Reflector unconformity. Stratigraphic intervals are indicated to the right of the seismic reflection section. The cyan dashed lines indicate boundaries of the chimney-like structures, labelled A, B and C. HP denotes a dominant pipe-like high velocity anomaly. H, TV and P1 marks corresponding features labelled in Fig. 8. Two vertical solid black lines show the boundaries of the inverted model. The red arrows indicate the positions of broken reflections suggestive of a deformed interface. The red and blue colours overlay show low and high velocity anomalies, respectively. The solid white lines show hit-count contour lines. (b) Interpretation of the velocity model superimposed on the stratigraphic intervals. The white open circles denote gas-bearing sediments and the grey dashed symbols denote high-velocity structures within the well-defined regions. The solid horizontal white lines show inversion cell height in TWT (Two-Way Traveltime) domain and dotted yellow boxes delineate extents of well-resolved areas used in estimation of *in situ* gas volumes (sub-section 9.3).

porosity expected for sandstones (Nur *et al.* 1998). On the other hand, the Scanner Pockmark is an active methane venting complex, and the amplitudes of the low-velocity structures are fairly similar to those of anomalies where we are confident about the presence of gas (compare the velocity anomalies appearing within the solid

cyan line with those between the two dashed cyan lines in Fig. 10b). So it is reasonable to attribute the low-velocity anomalies to the gas-charged sediments within the region. To further investigate the feasibility of gas-related anomalies, we used the Gassmann (1951) equation to assess the effect of replacing brine by methane in the

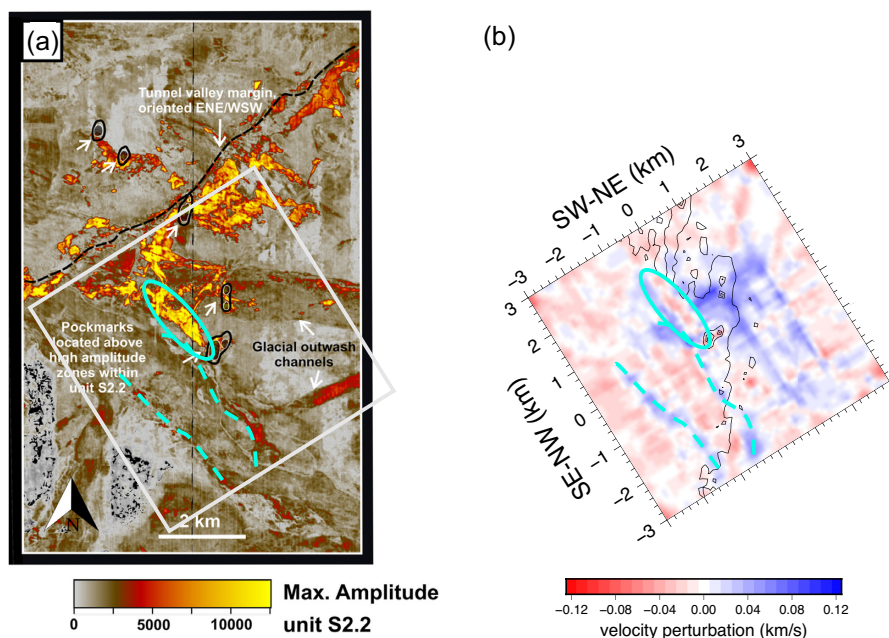


**Figure 10.** (a) Maximum amplitude map of the Ling Bank upper unit (S2.2) Fm. extracted using a window extended along full depth range of the unit (modified after Callow *et al.* 2021). The black lines show bathymetry contour lines, white arrows indicate glacial outwash channels and grey box marks boundaries of the velocity anomaly map illustrated in (b). (b) Corresponding velocity anomaly map at 200 mbsl. The red and blue colours denote low- and high-velocity zones. The cyan solid and dashed lines indicate position of corresponding features.

**Table 2.** Estimated bulk modulus and density of sediments and pore fluid contents at the representative depth of 50 mbsf (200 mbsl—pressure of 2 MPa bar and temperature of 8.5 °C) and 250 mbsf (400 mbsl—pressure of 4 MPa and temperature of 14.5 °C) at the Scanner Pockmark complex area. Water salinity is assumed 35 000 ppm.

	Depth (mbsl)	Quartz	Clay	Brine	Methane
Bulk Modulus (GPa)	200	36.6	21	2.26	0.0027
	400	–	–	2.33	0.0057
Density (g cm <sup>-3</sup> )	200	2.65	2.58	1.024	0.017
	400	–	–	1.024	0.036

unconsolidated marine sediments of the Coal Pit and Ling Bank Fm. For this purpose, we focused our assessment on the low-velocity anomaly of  $\sim 55 \text{ ms}^{-1}$  that is evident below the Scanner Pockmark location on the 200-mbsf map of Fig. 8. At this location, a well-constrained CSEM study was also carried out by Gehrman *et al.* (2021), as described in the introduction section. The CSEM-derived resistivity data can discriminate higher gas saturations more effectively than seismic data. We used the gas saturation, porosity and gas layer thickness information provided by Gehrman *et al.* (2021) to assess and calibrate our Gassmann models.

In our Gassmann model, porosity and clay content values are assumed to be constant and equal to 40 per cent and 70 per cent, respectively. The porosity is selected based on the porosity range reported by Gehrman *et al.* (2021), and the clay volume fraction is assumed to be 70 per cent to honour the clay-rich nature of the sediments (Graham *et al.* 2010; Stoker *et al.* 2011) and the Witch Ground Fm. core measurements (Falcon-Suarez *et al.* 2021). Table 2 shows bulk moduli and densities of the sediment and pore fluid contents at 50 mbsf depth (200 mbsl), corresponding to a location within the Coal Pit Fm. The pressure and temperature values at 50 mbsf are 2 MPa and 8.5 °C, which are derived assuming hydrostatic

pressure, an annual seabed temperature of 7 °C (Shell UK Limited 2014) and a geothermal gradient of 30 °C km<sup>-1</sup> (Harper 1971). Clay and quartz bulk moduli and densities are adopted from Mavko *et al.* (2009), and the pore fluid bulk moduli and densities are derived using the equation of Batzle & Wang (1992). The shear modulus and the frame bulk modulus of the dry rock are derived using shear and compressional velocity values reported by Robinson *et al.* (2022) at  $\sim 50$  mbsf ( $V_p = 1720 \text{ ms}^{-1}$ —i.e. consistent with the tomography result—and  $V_s = 310 \text{ ms}^{-1}$ , where  $V_s$  is estimated from  $V_p$  using the Castagna's empirical relationship for mudrocks; Castagna *et al.* 1985).

Our Gassmann model (black solid line in Fig. 11) calculates a velocity of  $\sim 820 \text{ ms}^{-1}$  for a gas saturation of 34 per cent, as estimated by Gehrman *et al.* (2021). To examine the reliability of the obtained Gassmann model, we back calculated the thickness of the gas-charged layer and compared that to the 30–40 m gas-layer thickness measured from high-resolution seismic reflection data (Gehrman *et al.* 2021). To this end, we followed the principle that the seismic wave traveltime must be identical for the corresponding inverted velocity model and the resistivity-derived model across the first 100 m of sediments below the seafloor—hereinafter referred to as the 'equal seismic traveltime constraint'. We assumed a resistivity-derived model as a stack of two layers including a 35-m gas-charged layer with velocity of 820 ms<sup>-1</sup> (the velocity at 34 per cent gas saturation on the black solid line in Fig. 11) and a 65-m thick water saturated layer with a seismic velocity of 1720 ms<sup>-1</sup> (the velocity at 0 per cent gas saturation on the black solid line in Fig. 11). The corresponding inverted velocity model has a 100 m-thick sediment layer with a seismic velocity of 1690 ms<sup>-1</sup> (averaged velocity derived by the first arrival traveltime tomography). This observation supports the presence of a  $\sim 3$  m-thick gas-charged layer, that is 7.5 to 10 per cent of the thickness suggested by a high-resolution seismic reflection data (Gehrman *et al.* 2021). A potential explanation for this discrepancy is that the clay-rich sediments of the CP and

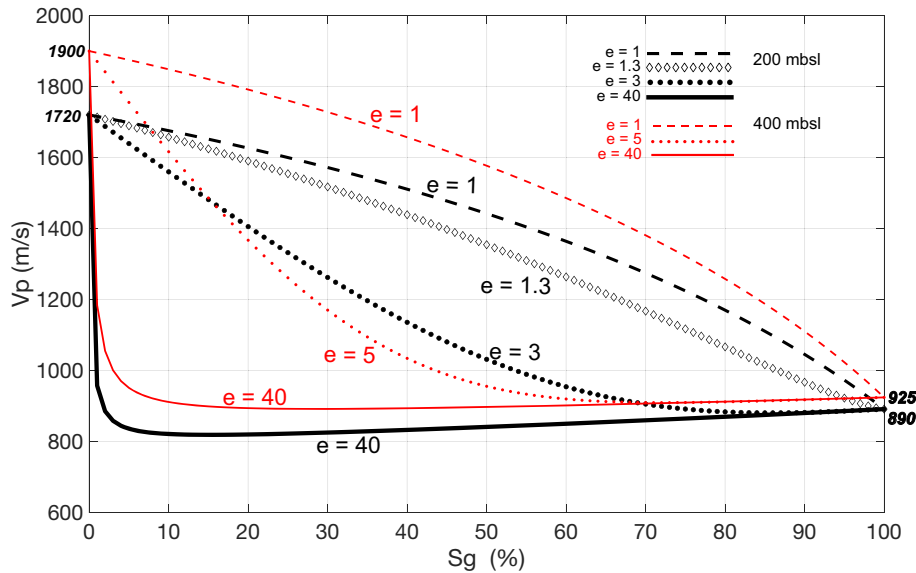


**Figure 11.** Compressional wave velocity ( $V_p$ ) as a function of gas saturation ( $S_g$ ) using Gassmann equation (solid lines) and patchy saturation–velocity relationship (dashed lines), derived for the depths of 200 (black colour) and 400 mbsl (green colour). Elastic moduli and densities used in Gassmann equation are given in Table 2. Porosity is assumed to be constant and equal to 40 per cent and 28 per cent for 200 and 400 mbsl, respectively, and the clay volume fraction is assumed 70 per cent for both depths. The letter ‘e’ denotes the Brie free parameter for each curve.

LB formations are prone to patchy gas saturation distribution, in contrast to the homogenous saturation assumption that we used in the Gassmann fluid substitution modelling. The patchy saturation scenario is also suggested through the lab experiment carried out by Falcon-Suarez *et al.* (2021) on two gravity core samples that are taken from  $\sim 1$  and  $\sim 2.1$  mbsf in the Witch Ground Fm. We used the equation of Brie *et al.* (1995) to calculate the effective bulk modulus of the pore fluid and modelled the patchy saturation–velocity relationship for the sediments underlying the Scanner Pockmark complex. Mavko & Mukerji (1998) showed that perfectly patchy (i.e. gas and water phases do not coexist at the same pore space and are separated by fully saturated patches) and homogeneous saturation correspond to the upper and lower bounds of velocity in partially saturated rock. To estimate the Brie free parameter ( $e$ ) for the Scanner Pockmark shallow sediments (0–100 mbsf depth-interval), we first estimated the gas saturation of the sediments by satisfying the equal gas volume per one square metre area within the CSEM and inverted velocity models—hereinafter referred to as the ‘volumetric constraint’. A 35-m-thick gas layer with a porosity of 30 per cent and 34 per cent gas saturation (average values for the gas pocket by Gehrman *et al.* 2021) results in an *in-situ* gas volume of  $\sim 3.57$  m<sup>3</sup> per square metre. To accommodate the same volume of gas within the 100-m-thick sediments with an average porosity of 40 per cent, we calculated a gas saturation of  $\sim 9$  per cent. Next, we calibrated the Brie free parameter by forcing the Gassmann model to pass through the point of 9 per cent gas saturation and 1665 ms<sup>-1</sup> velocity (i.e.  $-55$  ms<sup>-1</sup> velocity anomaly). The calibrated Brie free parameter was estimated to be 1.3 (Fig. 11, black diamond line). The corresponding saturation–velocity model indicates  $\sim 230$  ms<sup>-1</sup> velocity reduction at the average gas saturation of 34 per cent. Satisfying the equal seismic traveltimes constraint leads to an estimate of a  $\sim 22$  m-thick gas layer. This thickness is much closer to the gas layer thickness of 30–40 m from seismic reflection data, but still not satisfactory.

The presence of non-gas high-resistivity geological features, such as methane-derived authigenic carbonate, would constructively

contribute to the resistivity anomaly, leading to an overestimated CSEM-derived gas saturation. In contrast, this would result in underestimation of the velocity-derived gas saturation. To address the uncertainty associated with the presence of authigenic carbonate, we assumed the lower-end gas saturation of 20 per cent (Gehrman *et al.* 2021) and increased the low-velocity anomaly by 50 per cent to  $-80$  ms<sup>-1</sup>. The volumetric constraint suggested  $\sim 5$  per cent gas saturation. By passing the Gassmann model through the 5 per cent gas saturation and 1640 ms<sup>-1</sup> velocity ( $-80$  ms<sup>-1</sup> velocity anomaly) point, we readjusted the Brie’s free parameter to 3. The latter Brie free parameter also agrees well with that of the unconsolidated high-porosity marine sediments from offshore Oregon (Myung 2004), so is a realistic estimation. The new Gassmann model (Fig. 11, black dotted line) shows  $\sim 315$  ms<sup>-1</sup> velocity reduction at 20 per cent gas saturation. The latter Gassmann model also implies a  $\sim 22$  m-thick gas layer, required to realize the equal seismic traveltimes constraint.

At the other extreme, where the CSEM-derived gas saturation reaches to its upper-end of 48 per cent (Gehrman *et al.* 2021), we estimated a gas saturation of  $\sim 12.5$  per cent at the 55 ms<sup>-1</sup> velocity reduction. The corresponding new Brie free parameter suggests perfectly patchy saturation (Fig. 11, black dashed line) and a  $\sim 18$  m-thick gas layer.

In general, estimates of 9 and 12.5 per cent gas saturation are in reasonably good agreement with the reported maximum CO<sub>2</sub> saturation of  $10 \pm 5$  per cent measured for the muddy sediments of the Witch Ground Fm. at  $\sim 2.1$  mbsf (Falcon-Suarez *et al.* 2021), and  $10 \pm 3$  per cent CO<sub>2</sub> saturation at a depth of  $< 3$  mbsf for the Witch Ground Fm. obtained from the STEMM-CCS field release experiment data (Roche *et al.* 2021), although, the saturation can change with depth. We postulate that the small size of the authigenic carbonates (Böttner *et al.* 2019) limits their impact on the resistivity and velocity anomalies and the estimated 5 per cent gas saturation in the presence of authigenic carbonates is less likely.

Additionally, we model the Gassmann saturation–velocity relationship for the observed gas layer beneath the CR unconformity (400-mbsl map in Fig. 8a). At this depth, the petrophysical and

**Table 3.** Reservoir properties used to estimate the *in-situ* gas volumes within the gas-bearing sediments of the Ling Bank and the Nordland Group Fm.

Geological layer	Depth (mbsl)	Porosity (per cent)	Shale fraction (per cent)	Brie Constant (Gassmann modelling)	<i>In-situ</i> gas volume (106 m <sup>3</sup> )
Ling Bank Fm.	200	44	56	1	3.73
		40	70	1.3	1.64
		36	84	3	0.31
Nordland Group Fm.	400	34	55	1	3.16
		22	85	5	0.13

elastic parameters are poorly constrained, leading to a large uncertainty. We assumed the same clay volume fraction of 70 per cent as for the shallow depth and porosity of 28 per cent, close to the porosity range at 150 mbsf, estimated by Gehrman *et al.* (2021). Pressure and temperature at 400 mbsl (250 mbsf) are 4 MPa and 14.5 °C respectively (derived, as explained, for the shallow depth). The corresponding fluid's density and bulk modulus were estimated using the Batzle & Wang (1992) equations and are given in Table 2. The shear modulus and dry rock frame modulus were estimated using the averaged inverted compressional velocity at 400 mbsl (~1900 ms<sup>-1</sup>) and a corresponding shear wave velocity (460 ms<sup>-1</sup>) was estimated using the empirical relationship of Castagna *et al.* (1985). We assumed three saturation scenarios, namely, homogeneous saturation (Fig. 11, solid red line;  $e = 40$ ), perfectly patchy saturation (Fig. 11, dashed red line;  $e = 1$ ) corresponding to the upper gas saturation limit and partially patchy scenario (Fig. 11, dotted red line) with the Brie free parameter of 5, similar to that of the unconsolidated sediments of the Utsuia Formation at 800–1000 mbsl depths at the Sleipner CCS site (Williams & Chadwick 2021).

### 9.3 *in-situ* gas volume

Using our model, we can quantify the gas volume in layers above the glacial unconformity (combined Ling Bank and Coal Pit formations) and below the CR regional unconformity (Nordland Group). The areal extents of the gas-bearing zones were estimated from our inverted velocity model, confined to the well-resolved areas where the inversion cell ray hit-count is > 100. The gas saturation scenarios were estimated using the patchy saturation–velocity relationships that are derived in subsection 9.2 (Fig. 11). We also investigated the uncertainty associated with the input parameters, ignoring the interrelation between the input parameters (e.g. effect of porosity variation on a modeled saturation–velocity relationship) as the effects were minimal compared to the corresponding input variations. Table 3 summarizes the input parameters used in gas volume estimates and the results for each depth, and sections 9.3.1 and 9.3.2 elaborate on our choice of input parameters.

#### 9.3.1 Ling bank and coal pit formations

To estimate the area of the shallow gas-bearing zones we used a velocity cut-off value of 1720 ms<sup>-1</sup> (corresponding to the compressional wave velocity at 100 per cent water saturation, Fig. 11) at 200-mbsl depth in order to delineate the gas-charged zones. An area of ~8.45 km<sup>2</sup> was calculated. The gas volume was calculated for the base case scenario using the patchy gas saturation–velocity relationship shown by the black diamond line in Fig. 11, 40 per cent porosity and 70 per cent clay volume fraction. The upper and lower gas volume scenarios were also calculated assuming ±20 per cent variation in clay volume fraction, ±10 per cent variation in

porosity and the gas saturation–velocity relationships shown by the black dashed (upper case) and dotted (lower case) lines in Fig. 11. The *in-situ* gas volume for lower, base and upper case scenarios are about 0.31, 1.64 and 3.73 × 10<sup>6</sup> m<sup>3</sup>, respectively. Using the gas density of 0.017 g cm<sup>-3</sup> (Table 2), gas mass of corresponding scenarios are 5.27, 27.88 and 63.41 × 10<sup>6</sup> kg. Considering the methane mass flux rate of 1.6–2.7 × 10<sup>6</sup> kg yr<sup>-1</sup> (Li *et al.* 2020) at the Scanner Pockmark, the lower, base and upper case scenarios could sustain the observed gas flux for around 2–3, 10–17 and 23–40 yr. The presence of authigenic carbonate at the Scanner Pockmark complex (Judd & Hovland 2007; Robinson *et al.* 2021) suggests ongoing methane venting for several thousand years (Teichert *et al.* 2003), much longer than the estimated depletion time span of 2–40 yr. Thus these sediments must be continuously fed from deeper gas-rich strata to maintain the seabed methane seepage for thousands of years.

#### 9.3.2 Nordland group

The same procedure was repeated to estimate the *in-situ* gas volume underlying the Crenulate Reflector at 400 mbsl. Compared to the shallow sediments of the LB and CP Fm., gas volume estimation at this depth is less constrained because of the lack of measurements and reliable independent studies. The area of the gas-charged zone was estimated to be about 5.30 km<sup>2</sup> at 400 mbsl depth, defined using a velocity cut-off value of 1900 ms<sup>-1</sup>, corresponding to the compressional wave velocity at 100 per cent water saturation (Fig. 11). Assuming a porosity range of 22–34 per cent, clay volume fraction range of 55–85 per cent and the patchy gas saturation–velocity relationships shown by the red dotted (lower case) and dashed (upper case) lines in Fig. 11, an *in-situ* gas volume range of ~0.13–3.16 × 10<sup>6</sup> m<sup>3</sup> (~4.68–113.78 × 10<sup>6</sup> kg methane using the gas density of 0.036 g cm<sup>-3</sup>—Table 2) was calculated.

### 9.4 Gas migration pathway

The geometry of the low-velocity anomalies suggests that thermogenic methane (Clayton & Dando 1996) is migrating vertically through a major chimney (labelled P2 on 500-, 600- and 700-mbsl maps in Figs 8a and 12) within the Nordland Group, situated ~1 km south of the Scanner Pockmark. Additionally, gas migrates vertically through a smaller pipe-like structure evident below the Scanner Pockmark in the 500- and 600-mbsl maps in Fig. 8(a) (labelled P1 in Figs 8a and 12). The gas reaches the CR regional unconformity at the base of the Aberdeen Ground Fm. (corresponding to the 400-mbsl map in Fig. 8a), where it accumulates (denoted by G on 400-mbsl map in Figs 8a and 12), mixes with *in-situ* biogenic gas (Judd *et al.* 1994; Böttner *et al.* 2019) and spreads towards the NW (black arrow on 400-mbsl map in Fig. 12) along the possible regional migration pathway interpreted by Callow *et al.* (2021).

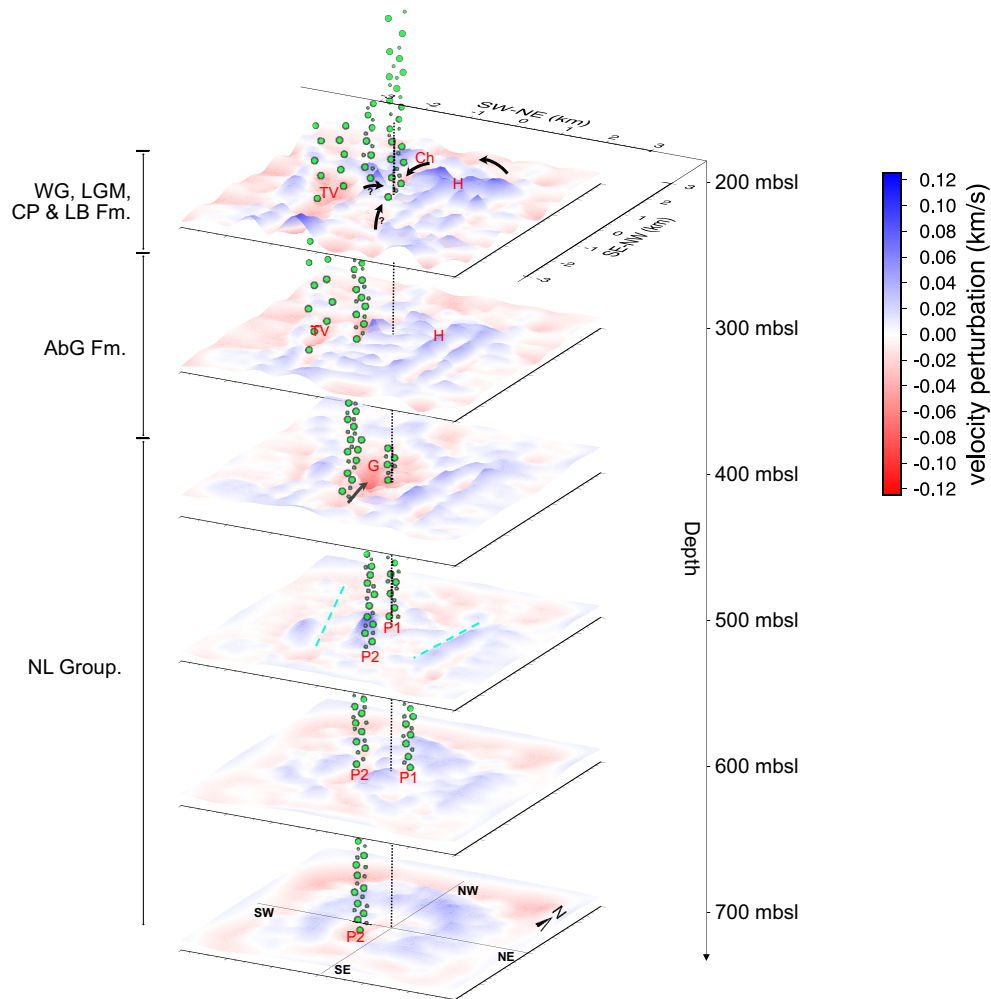


**Figure 12.** Schematic perspective of the gas migration paths underlying the Scanner Pockmark complex. The red-blue anomaly maps correspond to those illustrated in Fig. 8. The green bubbles demonstrate the interpreted vertical gas migration paths and the black arrows on maps at 200 and 400-mbsl indicate horizontal gas migration paths. The dotted vertical line shows the vertical projection line of the Scanner Pockmark location. The dashed cyan lines, and labels P1, P2, Ch, TV, H and G indicate corresponding features in Fig. 8. Stratigraphic intervals are indicated to the left of the figure.

The possible regional pathway has been inferred from the depth map of the Crenulate Reflector interpreted from 3-D seismic reflection data. The trapped gas under the Crenulate Reflector migrates upwards through the low velocity anomaly indicated by the black arrow in the 400-mbsl depth slice in Fig. 8(a) and reaches the SE–NW tunnel valley (labelled TV in the 300- and 200-mbsl maps in Figs 8a and 12). As discussed in section 9.1, the SE–NW tunnel valley may act as a conduit allowing the gas to migrate towards the glacial deposits overlying the Aberdeen Ground Formation. Our velocity model suggests several horizontal migration pathways (indicated by black arrows on 200-mbsl map in Fig. 12) towards the Scanner Pockmark and underlying shallow reservoirs of the Coal Pit and Ling Bank formations within the stratigraphic trap created by two intersecting SE–NW and SW–NE tunnel valleys (Callow *et al.* 2021). In particular, the narrow NW–SE channel at < 200 mbsl (labelled Ch on the 200-mbsl map in Figs 8a and 12) appears to be a major horizontal gas migration pathway towards the Scanner Pockmark complex, as interpreted by Callow *et al.* (2021) as well.

### 9.5 High-velocity anomalies

While the low-velocity anomalies at this study area can be attributed to the presence of gas-saturated porous sediments, interpretation of the inverted high-velocity zones remains ambiguous. The high-velocity anomalies are also evident in absolute velocity maps (Fig. 7a), suggesting they result from real geological features. Commonly, sediment compaction, porosity reduction, shale volume increase and lithology changes can cause high-velocity structures within sedimentary rocks. In addition, methane-derived authigenic carbonate (MDAC) cementation is a common phenomenon associated with focused fluid flow systems. Nevertheless, MDAC is expected to appear in the form of isolated small-scale anomalies (Böttner *et al.* 2019), whereas the high-velocity anomalies in this study have dimensions reaching several kilometres around and away from the chimney-like structure. Despite the uncertainties associated with the interpretation of these anomalies, plausible explanations for some of them can be developed by synthesizing information from various sources.

### 9.5.1 Linear high-velocity anomalies

As discussed in section 9.1, two narrowly elongated SE–NW high-velocity anomalies, indicated by dashed cyan lines in Fig. 10, are present along the edges of the SE–NW tunnel valley and suggest compaction of the host sediments. In addition, comparison with the maximum amplitude map (Fig. 10a) shows that the position of these anomalies partly overlaps the location of the relatively brightened amplitudes, a common feature associated with high velocity sediments (assuming the brightened reflections have normal polarity along the tunnel valley's rims).

### 9.5.2 Flat high-velocity anomalies

On the 200-mbsl map in Fig. 8(a), a dominant high-velocity anomaly zone (labelled H) is confined to the SE by the SE–NW tunnel valley, and to NW by the gas bearing sediments of Ling Bank Fm. (Fig. 10a). This anomaly extends down to the Aberdeen Ground Fm. (Fig. 8, 300-mbsl map). The Aberdeen Ground Fm. is interpreted as a sealing cap-rock formation by Böttner *et al.* (2019). Thus, porosity reduction and increased clay volume might explain this high velocity anomaly at 300 mbsl, but it remains indefinite at 200 mbsl.

### 9.5.3 Pipe-like high-velocity anomaly

In Fig. 9(a), a noticeable vertical high-velocity anomaly (labelled HP) is evident in the vicinity of the Scanner Pockmark towards the SW. This anomaly extends from ~300 ms TWT down to ~450 ms TWT, corresponding to ~250–350 mbsl. The anomaly can be tracked up to the seafloor, showing a ~300 m shift towards the NW on the 200-mbsl map in Fig. 8. The anomaly shows a maximum amplitude of +110 ms<sup>-1</sup> and resembles a subvertical pipe-like cemented chimney. We speculated that this might be a cemented chimney; however, this needs more evidence such as associated paleopockmarks to be confirmed.

### 9.5.4 Concentric high-velocity anomalies

At greater depth, the velocity model shows a nearly concentric high- and low-velocity pattern throughout the ~500 to ~700 mbsl interval (within the Nordland Group). This resembles a high-velocity dome-like structure embedded by low-velocity sediments. The high-velocity dome is also breached by several low velocity patches in different areas. We have shown plausibility of this interpretation through the synthetic test (Figs B2a and b, 600- and 700-mbsl maps); however, this cannot be confirmed without incorporation of independent information such as drilling data. A possible explanation of the extensive high-velocity zone within the Nordland Group is interbedded high-velocity limestone layers within the clay-rich strata that are interpreted using composite log and shallow seismic profiles (Judd *et al.* 1994).

## 10 CONCLUSIONS

From our high-resolution seismic velocity model of the region around the Scanner Pockmark complex, we conclude that:

(i) The chimney structure imaged by seismic reflection data is part of a larger complex fluid escape structure that hydraulically connects the strata at depths of > 700 mbsl to the seafloor via an indirect pathway. The venting gas at the Scanner Pockmark is being

fed vertically through indirect migration pathways and laterally through a narrow NW–SE shallow channel.

(ii) The part of the chimney-like seismic reflection anomaly that extends across the Aberdeen Ground Fm. is indeed an artefact generated by the overlying gas pockets of the Ling Bank and Coal Pit formations.

(iii) The integrated velocity- and resistivity-derived gas saturation study suggests that the gas across the sediments of Ling Bank and Coal Pit Fm. in the Scanner Pockmark region must be distributed in a patchy pattern with the Brie free parameter of 1.3, close to the perfectly patchy saturation upper bound.

(iv) Our estimated base-case gas volume across the Ling Bank and Coal Pit Fm. indicates that the current observed methane flux can last for about 10–17 yr, with less likely lower and upper time-scale scenarios spanning between 2 and 40 yr, therefore, this long-lived reservoir must be continuously replenished from below.

(v) The velocity model suggests that the SE–NW tunnel valley is a plausible vertical migration pathway connecting the accumulated gas under the CR to the porous sediment overlying the Aberdeen Ground Fm.

(vi) The linear high-velocity anomalies that correlate with the rims of the NW–SE tunnel valley, suggest compaction of host sediments during creation of the tunnel valley.

(vii) A plausible migration path of the thermogenic gas is a cylindrical chimney structure within the Nordland Group situated ~1–1.5 km towards the SE of the Scanner Pockmark.

## ACKNOWLEDGMENTS

This work was funded by the Natural Environment Research Council (CHIMNEY; NERC Highlight Topic; NE/N016130/1 and NE/N015762/1) and also has received funding from the European Union's Horizon 2020 research and innovation programme under grant agreement No. 654462 (STEMM-CCS). For the purpose of open access, the author has applied a CC BY public copyright licence to any Author Accepted Manuscript version arising from this submission. The NERC Ocean-Bottom Instrumentation Facility (Minshull *et al.* 2005) provided the OBSs and their technical support at sea during JC152. We would like to thank all those involved in the planning and acquisition of data during RRS James Cook cruise JC152, including the officers, engineers and crews, the scientific parties and all seagoing technicians and engineers. We thank Andrew Gorman and an anonymous reviewer for their helpful and constructive comments.

**Software Availability:** FAST codes can be downloaded from the Rice University website at <https://terra.rice.edu/departement/faculty/zelt/fast.html>.

## DATA AVAILABILITY

All project data have been archived by the British Oceanographic Data Centre (BODC). OBS data used in this study are available at <http://dx.doi.org/10.5285/0068C20ACA6C43E786E737C9257179A2>.

## REFERENCES

Andresen, K.J., 2012. Fluid flow features in hydrocarbon plumbing systems: what do they tell us about the basin evolution?, *Mar. Geol.*, **332–334**, 89–108.

- Andresen, K.J., Huuse, M. & Clausen, O.R., 2008. Morphology and distribution of Oligocene and Miocene pockmarks in the Danish North Sea—implications for bottom current activity and fluid migration, *Basin Res.*, **20**(10), 445–466.
- Andresen, K.J., Dahlin, A., Kjeldsen, K.U., Røy, H., Bennike, O., Nørgaard-Pedersen, N. & Seidenkrantz, M.-S., 2021. The longevity of pockmarks—a case study from a shallow water body in Northern Denmark, *Mar. Geol.*, **434**, 106440.
- Arntsen, B., Wensaas, L., Løseth, H. & Hermanrud, C., 2007. Seismic modeling of gas chimneys, *Geophysics*, **72**(5), SM251–SM259.
- Avseth, P., Mukerji, T. & Mavko, G., 2005. Introduction to rock physics, in *Quantitative Seismic Interpretation: Applying Rock Physics Tools to Reduce Interpretation Risk*, pp. 1–47, Cambridge Univ. Press.
- Batzle, M.L. & Wang, Z., 1992. Seismic properties of pore fluids, *Geophysics*, **57**, 1396–1408.
- Bayrakci, G. *et al.*, 2021. Seismic anisotropy within an active fluid flow structure: scanner Pockmark, North Sea, *Front. Earth Sci.*, **9**(May), 1–16.
- Berndt, C., 2005. Focused fluid flow in passive continental margins, *Phil. Trans. A: Math. Phys. Eng. Sci.*, **363**(1837), 2855–2871.
- Böttner, C. *et al.*, 2019. Pockmarks in the Witch Ground Basin, Central North Sea, *Geochem. Geophys. Geosyst.*, **20**(4), 1698–1719.
- Brie, A., Pampuri, F., Marsala, A.F. & Meazza, O., 1995. Shear sonic interpretation in gas-bearing sands, in *SPE Annu. Techn. Conf. Exhibit., Dallas, Texas, October 1995, SPE-30595-MS*, pp. 701–710, ATCE, doi: 10.2118/30595-MS
- Brown, K.M., 1990. The nature and hydrogeologic significance of mud diapirs and diatremes for accretionary systems, *J. geophys. Res.*, **95**(B6), 8969–8982.
- Bull, J.M., 2018. Cruise Report RRS James Cook 152 - JC152: CHIMNEY—Characterization of major overburden pathways above sub-seafloor CO<sub>2</sub> storage reservoirs in the North Sea. *Scanner and Challenger Pockmark Complexes*, University of Southampton.
- Callow, B. *et al.*, 2021. Seismic chimney characterisation in the North Sea—implications for pockmark formation and shallow gas migration, *Mar. Pet. Geol.*, **133**, 105301.
- Cartwright, J., Huuse, M. & Aplin, A., 2007. Seal bypass systems, *AAPG Bull.*, **91**, 1141–1166.
- Cartwright, J. & Santamarina, C., 2015. Seismic characteristics of fluid escape pipes in sedimentary basins: implications for pipe genesis, *Mar. Pet. Geol.*, **65**, 126–140.
- Castagna, J.P., Batzle, M.L. & Eastwood, R.L., 1985. Relationships between compressional-wave and shear-wave velocities in clastic silicate rocks, *Geophysics*, **50**(4), 571–581.
- Cathles, L.M., Su, Z. & Chen, D., 2010. The physics of gas chimney and pockmark formation, with implications for assessment of seafloor hazards and gas sequestration, *Mar. Pet. Geol.*, **27**(1), 82–91.
- Clayton, C.J. & Dando, P.R., 1996. Comparison of seepage and seal leakage rates, in *Hydrocarbon Migration and Its Near-Surface Expression*, vol. **66**, pp. 169–171, eds Schumacher, D. & Abrams, M. A., American Association of Petroleum Geologists.
- Constable, S., Orange, A. & Key, K., 2015. And the geophysicist replied: “Which model do you want?”, *Geophysics*, **80**(3), E197–E212.
- Dando, P.R. *et al.*, 1991. Ecology of a North Sea pockmark with an active methane seep, *Mar. Ecol. Prog. Ser.*, **70**(1), 49–63.
- Davies, R.J., 2003. Kilometer-scale fluidization structures formed during early burial of a deep-water slope channel on the Niger Delta, *Geology*, **31**(11), 949–995.
- Davies, R.J., Mathias, S.A., Moss, J., Hustoft, S. & Newport, L., 2012. Hydraulic fractures: how far can they go?, *Mar. Pet. Geol.*, **37**(1), 1–6.
- Falcon-Suarez, I.H. *et al.*, 2021. Core-scale geophysical and hydromechanical analysis of seabed sediments affected by CO<sub>2</sub> venting, *Int. J. Greenhouse Gas Control*, **108**, 103332.
- Gassmann, F., 1951. Ueber die Elastizität poröser Medien: vier. der Natur, *Gesellschaft Zürich*, **96**, 1–23.
- Gay, A., Lopez, M., Cochonat, P., Sultan, N., Cauquil, E. & Brigaud, F., 2003. Sinuous pockmark belt as indicator of a shallow buried turbiditic channel on the lower slope of the Congo basin, West African margin, *Geol. Soc. Lond. (Special Publications)*, **216**(1), 173–189.
- Gay, A., Lopez, M., Cochonat, P., Séranne, M., Levaché, D. & Sermondadaz, G., 2006. Isolated seafloor pockmarks linked to BSRs, fluid chimneys, polygonal faults and stacked Oligocene–Miocene turbiditic palaeochannels in the Lower Congo Basin, *Mar. Geol.*, **226**(1), 25–40.
- Gehrmann, R. *et al.*, 2021. Porosity and free gas estimates from controlled source electromagnetic data at the Scanner Pockmark in the North Sea, *Int. J. Greenhouse Gas Control*, **109**, 103343.
- Graham, A.G.C., Lonergan, L. & Stoker, M.S., 2010. Depositional environments and chronology of Late Weichselian glaciation and deglaciation in the central North Sea, *Boreas*, **39**(3), 471–491.
- Graue, K., 2000. Mud volcanoes in deepwater Nigeria, *Mar. Pet. Geol.*, **17**(8), 959–974.
- Han, D., Nur, A. & Morgan, D., 1986. The effects of porosity and clay content on wave velocities in sandstones, *Geophysics*, **52**(4), 583–583.
- Harper, M.L., 1971. Approximate geothermal gradients in the north sea basin, *Nature*, **230**(5291), 235–236.
- Hole, J.A. & Zelt, B.C., 1995. 3-D finite-difference reflection travel times, *Geophys. J. Int.*, **121**(2), 427–434.
- Hovland, M., Gardner, J.V. & Judd, A.G., 2002. The significance of pockmarks to understanding fluid flow processes and geohazards, *Geofluids*, **2**(2), 127–136.
- Hubbert, M.K. & Willis, D.G., 1957. Mechanics of hydraulic fracturing, *Trans. Soc. Petrol. Eng. AIME*, **210**(01), 153–163.
- Huuse, M., Jackson, C.A.L., Van Rensbergen, P., Davies, R.J., Flemings, P.B. & Dixon, R.J., 2010. Subsurface sediment remobilization and fluid flow in sedimentary basins: an overview, *Basin Res.*, **22**(4), 342–360.
- Judd, A., Long, D. & Sankey, M., 1994. Pockmark formation and activity, U.K. block 15/25, North Sea, *Bull. Geol. Soc. Denmark*, **41**, 34–49.
- Judd, A.G. & Hovland, M., 2007. *Seabed Fluid Flow: The Impact of Geology, Biology and the Marine Environment*, Cambridge Univ. Press.
- Karstens, J. & Berndt, C., 2015. Seismic chimneys in the Southern Viking Graben—implications for paleo fluid migration and overpressure evolution, *Earth planet. Sci. Lett.*, **412**, 88–100.
- Kissling, E., Ellsworth, W.L., Eberhart-Phillips, D. & Kradolfer, U., 1994. Initial reference models in local earthquake tomography, *J. geophys. Res.: Solid Earth*, **99**, (B10), 19 635–19 646.
- Leifer, I. & Boles, L., 2005. Measurement of marine hydrocarbon seep flow through fractured rock and unconsolidated sediment, *Mar. Pet. Geol.*, **22**(4), 551–568.
- Li, J., Roche, B., Bull, J.M., White, P.R., Leighton, T.G., Provenzano, G., Dewar, M. & Henstock, T.J., 2020. Broadband Acoustic Inversion for Gas Flux Quantification-Application to a Methane Plume at Scanner Pockmark, Central North Sea, *J. geophys. Res.: Oceans*, **125**(9),
- Løseth, H., Gading, M. & Wensaas, L., 2009. Hydrocarbon leakage interpreted on seismic data, *Mar. Pet. Geol.*, **26**(7), 1304–1319.
- Løseth, H., Wensaas, L., Arntsen, B., Hanken, N., Basire, C. & Graue, K., 2011. 1000 m long gas blow-out pipes, *Mar. Pet. Geol.*, **28**(5), 1047–1060.
- MacDonald, I.R., Leifer, I., Sassen, R., Stine, P., Mitchell, R. & Guinasso, N., 2002. Transfer of hydrocarbons from natural seeps to the water column and atmosphere, *Geofluids*, **2**(2), 95–107.
- Mandl, G. & Harkness, R.M., 1987. Hydrocarbon migration by hydraulic fracturing, *Geol. Soc. Lond. (Special Publications)*, **29**(1), 39–53.
- Mavko, G. & Mukerji, T., 1998. Bounds on low-frequency seismic velocities in partially saturated rocks, *Geophysics*, **63**, 918–924.
- Mavko, G., Mukerji, T. & Dvorkin, J., 2009. *Rock Physics Handbook—Tools for Seismic Analysis in Porous Media*, Cambridge Univ. Press.
- Minshull, T.A., Sinha, M.C. & Peirce, C., 2005. Multi-disciplinary, sub-seabed geophysical imaging – a new pool of 28 seafloor instruments in use by the United Kingdom Ocean Bottom Instrument Consortium, *Sea Technol.*, **46**(10), 27–31.
- Moss, J.L. & Cartwright, J., 2010. 3D seismic expression of km-scale fluid escape pipes from offshore Namibia, *Basin Res.*, **22**(4), 481–501.
- Myung, W.L., 2004. Elastic velocities of partially gas saturated unconsolidated sediments, *Mar. Pet. Geol.*, **21**(6), 641–650.
- Nur, A., Mavko, G., Dvorkin, J. & Galmudi, D., 1998. Critical porosity: a key to relating physical properties to porosity in rocks, *Leading Edge*, **17**, 357–362.

- Plaza-Faverola, A., Westbrook, G.K., Ker, S., Exley, R.J.K., Gailler, A., Minshull, T.A. & Broto, K., 2010. Evidence from three-dimensional seismic tomography for a substantial accumulation of gas hydrate in a fluid-escape chimney in the Nyegga pockmark field, offshore Norway, *J. geophys. Res.: Solid Earth*, **115**(B8), B08104. doi: 10.1029/2009JB007078.
- Räss, L., Simon, N.S.C. & Podladchikov, Y.Y., 2018. Spontaneous formation of fluid escape pipes from subsurface reservoirs, *Sci. Rep.*, **8**, 11116.
- Robinson, A.H., Bayrakci, G., Macdonald, C., Minshull, T.A., Bull, J.M., Chapman, M., Henstock, T.J. & Callow, B., 2022. Constraints on fluid flow pathways from shear-wave splitting in and around an active fluidescape structure: scanner Pockmark, North Sea, *Geophys. J. Int.*, **231**(2), 1164–1195.
- Robinson, A.H. et al., 2021. Multiscale characterisation of chimneys/pipes: fluid escape structures within sedimentary basins, *Int. J. Greenhouse Gas Control*, **106**, 103245.
- Roche, B. et al., 2021. Time-lapse imaging of CO<sub>2</sub> migration within near-surface sediments during a controlled sub-seabed release experiment. *Int. J. Greenhouse Gas Control*, **109**, 103363.
- Ruge, S.M., Scarselli, N. & Bilal, A., 2020. 3D seismic classification of fluid escape pipes in the western Exmouth Plateau, North West Shelf of Australia, *J. geol. Soc.*, **178**, jgs2020–096.
- Schramm, B., Berndt, C., Dannowski, A., Böttner, C., Karstens, J. & Elger, J., 2021. Seismic imaging of an active fluid conduit below Scanner Pockmark, Central North Sea, *Mar. Pet. Geol.*, **133**, 105302.
- Shell UK Limited, 2014. *Peterhead CCS Project—Well Completion Concept Select Report*, PCCS-05-PT-ZW-7180-00003.
- Stewart, M.A. & Lonergan, L., 2011. Seven glacial cycles in the middle-late Pleistocene of northwest Europe: geomorphic evidence from buried tunnel valleys, *Geology*, **39**(3), 283–286.
- Stoker, M.S., Balson, P.S., Long, D. & Tappin, D.R., 2011. *An overview of the lithostratigraphical framework for the Quaternary deposits on the United Kingdom continental shelf* British Geological Survey Research Report, RR/11/03, 48pp.
- van der Hilst, R. & Spakman, W., 1989. Importance of the reference model in linearized tomography and images of subduction below the Caribbean Plate, *Geophys. Res. Lett.*, **16**, 1093–1096.
- Teichert, B.M.A., Eisenhauer, A., Bohrmann, G., Haas-schramm, A., Bock, B. & Linke, B., 2003. U/Th systematics and ages of authigenic carbonates from Hydrate Ridge, Cascadia Margin: recorders of fluid flow variations, *Geochim. cosmochim. Acta.*, **67**(20), 3845–3857.
- Williams, G.A. & Chadwick, R.A., 2021. Influence of reservoir-scale heterogeneities on the growth, evolution and migration of a CO<sub>2</sub> plume at the Sleipner Field, Norwegian North Sea, *Int. J. Greenhouse Gas Control*, **106**, 103260.
- Yarushina, V.M., Wang, L.H., Connolly, D., Kocsis, G., Fæstø, I., Polteau, S. & Lakhlifi, A., 2021. Focused fluid-flow structures potentially caused by solitary porosity waves, *Geology*, **50**(2), 179–183.
- Zelt, C.A. & Barton, P.J., 1998. Three-dimensional seismic refraction tomography: a comparison of two methods applied to data from the Faeroe Basin, *J. geophys. Res.: Solid Earth*, **103**(B4), 7187–7210.
- Zelt, C.A., Azaria, A. & Levander, A., 2006. 3D seismic refraction travel-time tomography at a groundwater contamination site, *Geophysics*, **71**(5), H67–H78.

## APPENDIX A: DATA UNCERTAINTY ANALYSIS

The traveltime pick uncertainty for each OBS was evaluated based on time difference statistics of adjacent shots around the survey-line intersections (i.e. cross-over analysis). Since the shot positions do not necessarily coincide at the line intersections, we selected shot pairs with less than 10 m separation for the analysis. However, the spacing between these nearly coincident shot pairs introduces an extra traveltime difference that interferes with the picks' uncertainty. The shot pair spacing related time difference can be estimated

and removed using a data-driven approach. To this end, we measured traveltime differences of consecutive shots on selected survey lines, having good signal-to-noise ratio, and plotted the measured time differences against corresponding shot-receiver offsets. Next, a least-squares regression line was fitted to the data. The regression line models the time delay between pairs of consecutive shots with  $19 \pm 0.5$  m spacing as a function of source–receiver offset. The regression line has a correlation coefficient of 0.88 for 95 per cent of data excluding outliers and 0.79 for the entire data set. Using the regression line, time corrections for selected shot pairs can be estimated using the following equation:

$$dt = \left( \frac{dx}{19} \right) \times dT_m,$$

where  $dt$  is the estimated time difference of two nearly coinciding shot pairs at a given source–receiver offset,  $dx$  is spacing between two nearly coinciding shot pairs and  $dT_m$  is the measured traveltime difference of consecutive shot pairs with a  $19 \pm 0.5$  m spacing at corresponding source–receiver offset. Fig. A1 displays traveltime difference histograms before and after the correction for picks from all OBSs. The corrected histogram shows a typical normal distribution, characteristic of remaining random error.

## APPENDIX B: SYNTHETIC TEST

A synthetic test was carefully designed based on preliminary inversion results and known limitations associated with the data and modelling. The primary aim of testing was to investigate the feasibility of retrieving velocity anomaly structures similar to those retrieved from our real data. The synthetic acquisition geometry matched that used in our experiment at Scanner Pockmark. The synthetic velocity model was generated by superimposing various high- and low-velocity anomalies on a 1-D background model. The background model was generated by horizontally averaging the 3-D starting model that is used in our field data inversion. The anomalies include structures in the form of a pipe, a channel, a horizontal layer and a dome, with different sizes, depths and anomaly magnitudes (Table B1).

Synthetic traveltimes were generated through each model using FAST's forward ray tracing algorithm. In addition, a normally distributed random noise with zero mean and a standard deviation of 2 ms (to mimic the real data uncertainty) was added to the synthetic data. The starting model was the 1-D average of the synthetic model. The forward node and inverse cell sizes, and the parameters  $\alpha$  and  $s_z$  were set to match the real data inversion parameters. The data uncertainty was set to 2 ms to honour the added noise. Initial RMS traveltime misfit and  $\chi^2$  for synthetic model are 7.3 ms and 13.4, respectively. After 10 iterations, they reached values of 2.3 ms and 1.4, respectively. Convergence was very slow after the 7th iteration and the inversion was stopped after 10 iterations.

Comparison of the inverted and true models (Fig. B2) shows that the inversion is able to reconstruct velocity anomalies with horizontal dimensions as small as 200 m at depths less than  $\sim 250$  mbsl and as small as 400 m down to  $\sim 500$  mbsl. However, at depths  $> 300$  mbsl artefacts start to emerge and smear the boundaries of the structures along ray paths. The synthetic test also showed that wide structures with thickness  $< 100$  m are unlikely to be retrieved and structures beyond 500 mbsl depth are strongly smoothed. Inverted anomaly amplitudes are reasonably similar to those of corresponding real ones down to  $\sim 350$  mbsl, but start to decrease as depth increases. In a few places on the 500 mbsl map, the inverted anomaly shows higher amplitudes than the real ones; this could be

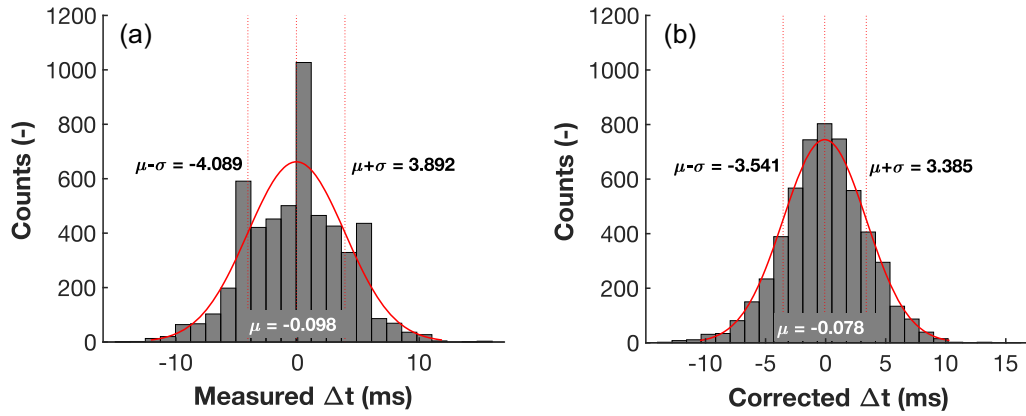


**Figure A1.** (a) Histogram of first-arrival traveltime differences of selected shot pairs (with < 10 m spacing) at seismic line intersections. (b) Histogram of the data following application of the correction for the time difference due to the spacing between selected shot pairs. The red curved lines show normal distribution fit to the corresponding data. Mean and standard deviation values are labelled for measured and corrected data residuals on corresponding graphs.

**Table B1.** Synthetic anomaly structures' descriptions.

Anomaly type	Amplitude ( $\text{m s}^{-1}$ )	Top (mbsl)	Base (mbsl)	Thickness (m)	Centre Coordinate —X/Y (m)	Diameter/Width/ Dimension—X × Y (m)
layer	-50	150	250	100	-1650/0	2200 × 6
channel	-100	150	250	100	-	200 × 2923
pipe	-100	150	250	100	0/0	200
layer	+100	250	310	60	0/0	6000 × 6000
pipe	-150	250	310	60	-500/0	400
Cone	-50	310	420	110 @ centre	0/-1000	2000 @ top -250 @ bottom
anticline	+100	600	800 @ edges	so	0/0	6000 × 6000
dome	-50	800 @ centre	800	150 @ centre	0/0	6000 × 6000
pipe	+100	150	2000	2000	500/0	400
pipe	-100	310	600	290	0/0	400
pipe	-150	310	2000	1690	0/-1000	1000

due to interference of leaking artefacts from the lower layers with real structures.

In addition, we investigated the effect of overestimating the data errors. Stopping at a misfit level that is too large clearly compromises the resolution of inverted model (compare Figs B2b and B3a) and results in large variations of the mean misfit with offset (Fig. B1b), as seen with our inversions of real data.

### APPENDIX C: DATA RESIDUALS AS A FUNCTION OF OFFSET

Averaged final velocities of the Monte–Carlo simulation resulted in an unsatisfactory RMS error of traveltime as a function of offset, showing strong bias in the far-offset region (Fig. C1a). To correct for the bias at far-offset, we applied a depth-variant linear scalar to the depths below the seafloor and obtained a reasonable error

distribution at all offsets (Fig. C1b). The scaling factor is  $(1 + \frac{i}{6500})$  that was defined through a trial- and -error approach.  $i$  represents the forward grid index starting from 1 at the first cell below the bathymetry depth and increases by 1 at every 10 m depth step (i.e. forward cell height).

### APPENDIX D: EFFECT OF REGULARIZATION PARAMETERS ON THE INVERSION RESULT

We used the 3-D starting model and explored the model space by testing several values of the parameters  $\alpha$  and  $s_z$  within reasonable ranges (i.e.  $0.5 \leq \alpha \leq 0.9$  and  $0.1 \leq s_z \leq 0.3$ ). All inverted models showed comparable results (Fig. D1). Thereafter, we set  $\alpha$  and  $s_z$  equal to 0.9 and 0.1, respectively, for all inversions.

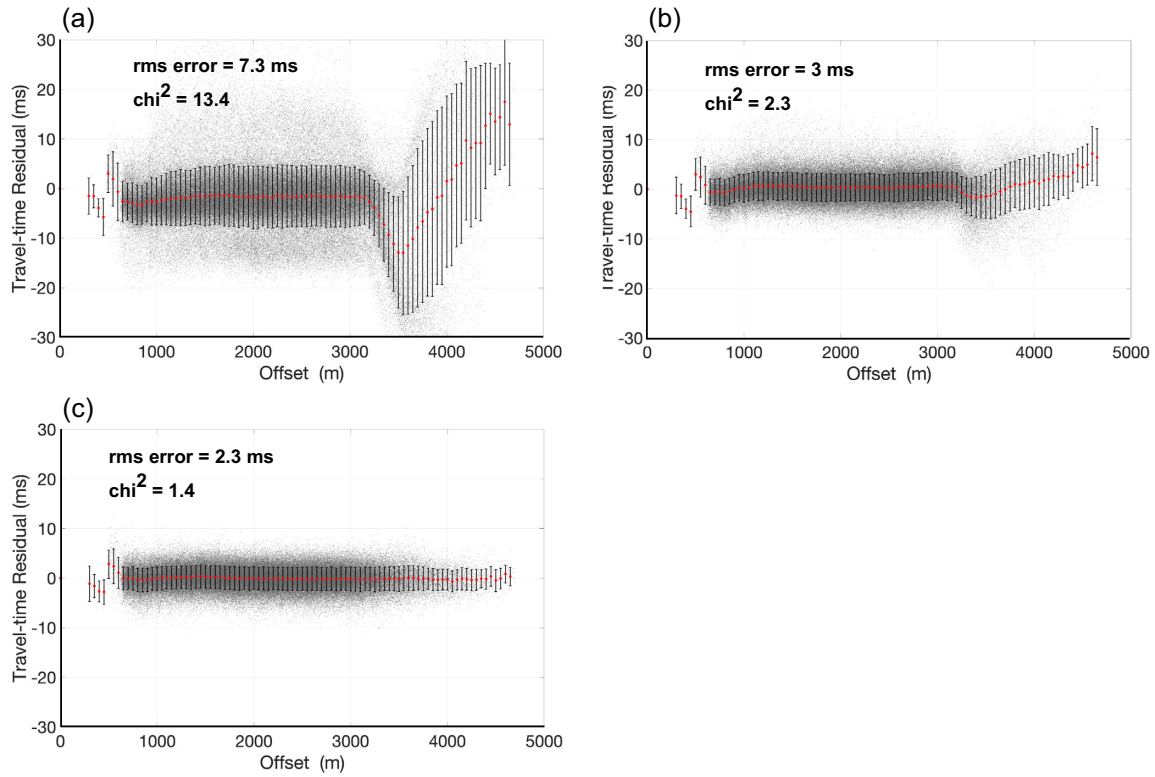


**Figure B1.** Traveltime residuals for the synthetic initial model (a) and inverted models with the RMS traveltime misfit of 3 (b) and 2.3 ms (c) as a function of source–receiver offset. The RMS error and  $\chi^2$  (normalized chi-squared) for each model are labelled on residual–offset plots. The grey dots show individual residuals and vertical black lines show one standard deviation error bar for residuals within 50-m offset bins.

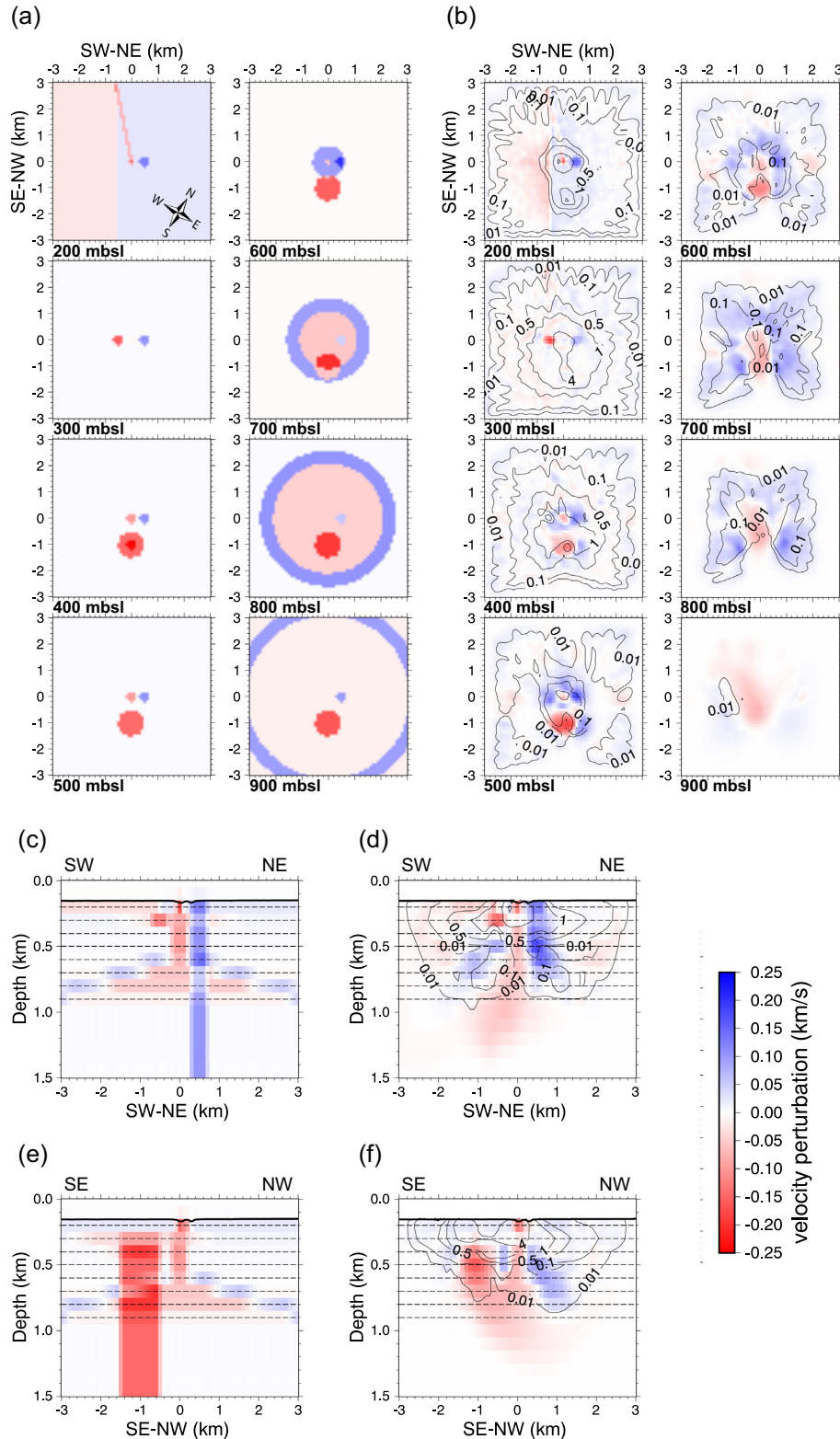


**Figure B2.** (a) Map views showing anomaly structures of the synthetic model (synthetic model–1-D average of starting model) at 100 m depth intervals from 200 to 900 m depth below sea level. 200 m depth corresponds to the shallowest inverted cell. (b) Map views showing corresponding inverted synthetic anomaly structures (inverted synthetic model–1-D average of starting model). (c, e) SW–NE and SE–NW cross sections passing through the chimney structure in the middle of the synthetic model. (d, f) corresponding SW–NE and SE–NW cross sections passing through the inverted synthetic model anomalies (inverted synthetic model–1-D average of starting model). The dashed black lines indicate depths of anomaly maps shown in (a) and (b). The red and blue colours denote low and high velocity zones, respectively. The solid black lines show hit-count contour lines (annotations are in  $10^3$ ).

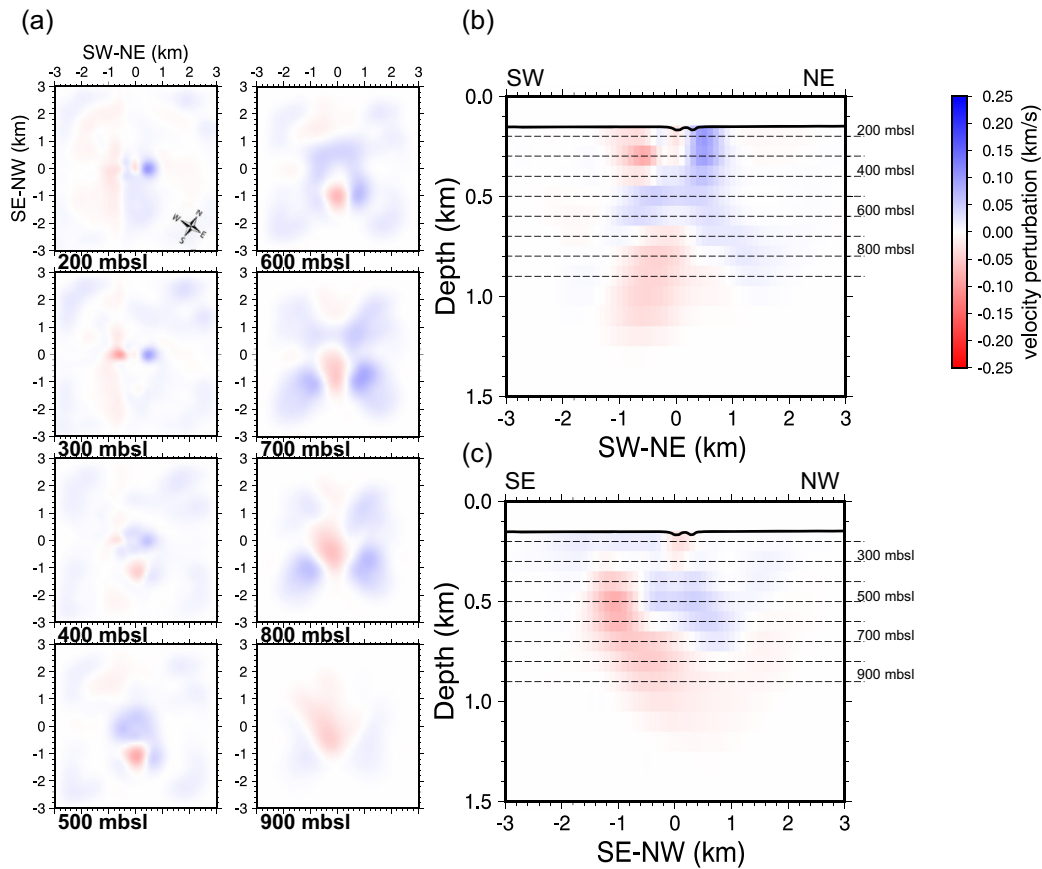


**Figure B3.** Map view (a) and cross sections (b, c) of inverted synthetic anomaly structures (inverted synthetic model–1-D average of starting model). The inverted model has RMS residual misfit of 3 ms and  $\chi^2$  of 2.3. Other details are as in Fig. B2.

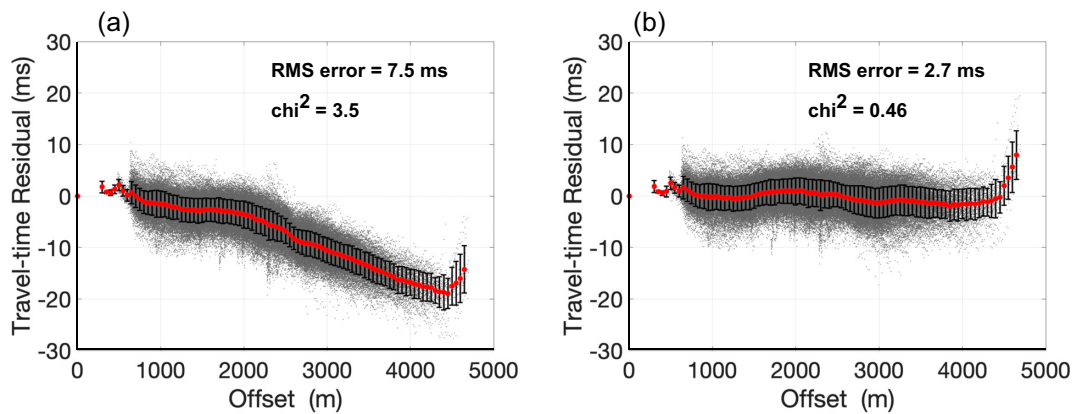


**Figure C1.** Traveltime residuals for 3-D average model (a) and scaled 3-D average model (using a depth-variant scaling) as a function of source–receiver offset. The grey dots show individual data residuals and vertical black lines show error bars (68 per cent confidence limit) for residuals within 50-m offset bins. Chi-squared values are calculated at 4 ms uncertainty level.

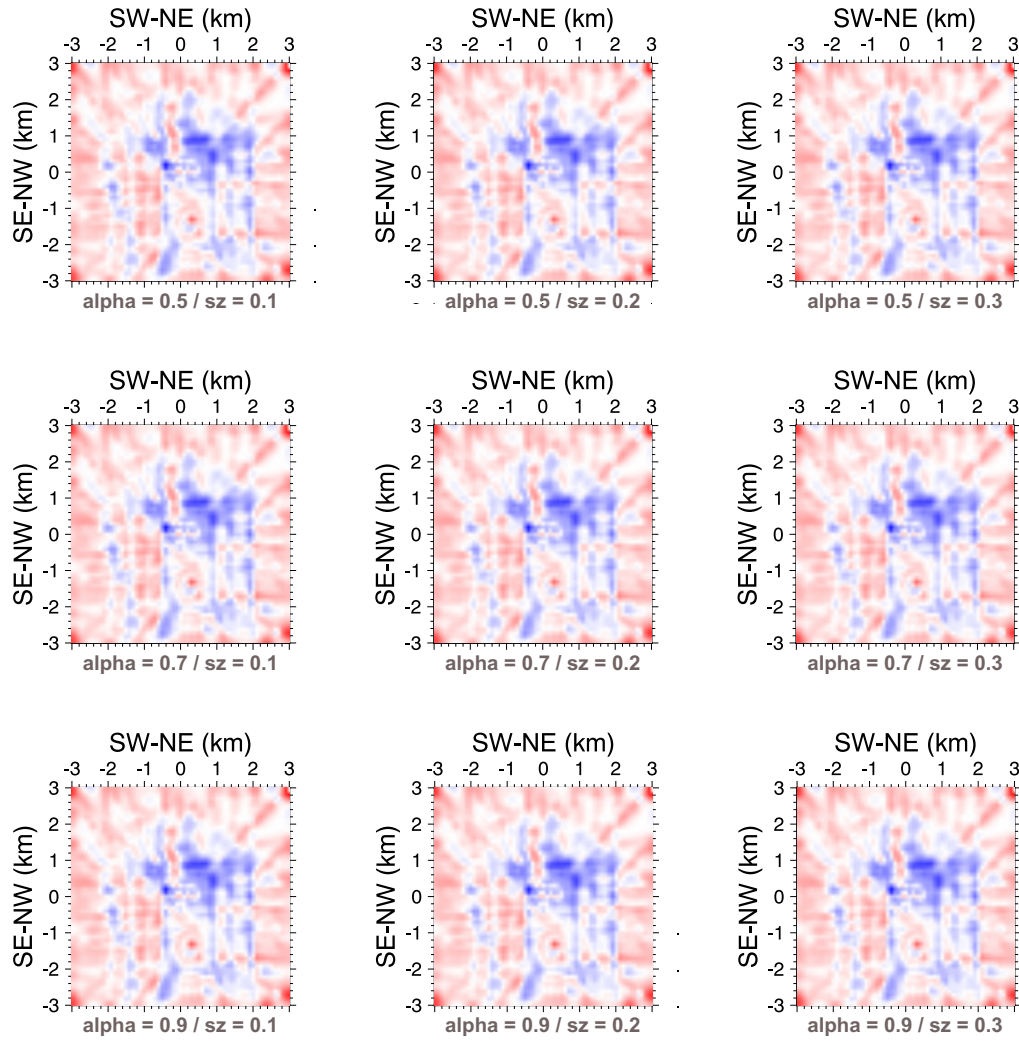


**Figure D1.** Velocity anomaly at 200 mbsl depth. The data are inverted using the 3-D starting model.  $\alpha$  and  $s_z$  parameters are varied between 0.5 to 0.9 and 0.1 to 0.3, respectively.